KeAi

CHINESE ROOTS
GLOBAL IMPACT

#### Contents lists available at ScienceDirect

# Petroleum Science

journal homepage: www.keaipublishing.com/en/journals/petroleum-science



# Original Paper

# Insight into evolution of invasive patterns on fingering phenomenon during immiscible two-phase flow through pore structure



Yu Li <sup>a, b, \*</sup>, Hui-Qing Liu <sup>a</sup>, Chao Peng <sup>a</sup>, Peng Jiao <sup>c</sup>, Wai Lam Loh <sup>b</sup>, Qing Wang <sup>a</sup>

- <sup>a</sup> State Key Laboratory of Petroleum Resources and Engineering, China University of Petroleum, Beijing, 102249, China
- <sup>b</sup> Department of Mechanical Engineering, National University of Singapore, 117575, Singapore
- <sup>c</sup> Oil and gas production Business Department, Kunlun Shuzhi Technology Co., LTD, Beijing, 100040, China

#### ARTICLE INFO

# Article history: Received 5 January 2024 Received in revised form 13 May 2024 Accepted 15 May 2024 Available online 16 May 2024

Edited by Yan-Hua Sun

Keywords: Immiscible two-phase flow Fingering phenomenon Invasive pattern Capillary number Parameters optimization

#### ABSTRACT

Understanding fingering, as a challenge to stable displacement during the immiscible flow, has become a crucial phenomenon for geological carbon sequestration, enhanced oil recovery, and groundwater protection. Typically governed by gravity, viscous and capillary forces, these factors lead invasive fluids to occupy pore space irregularly and incompletely. Previous studies have demonstrated capillary numbers, describing the viscous and capillary forces, to quantificationally induce evolution of invasion patterns. While the evolution mechanisms of invasive patterns have not been deeply elucidated under the constant capillary number and three variable parameters including velocity, viscosity, and interfacial tension. Our research employs two horizontal visualization systems and a two-phase laminar flow simulation to investigate the tendency of invasive pattern transition by various parameters at the pore scale. We showed that increasing invasive viscosity or reducing interfacial tension in a homogeneous pore space significantly enhanced sweep efficiency, under constant capillary number. Additionally, in the fingering crossover pattern, the region near the inlet was prone to capillary fingering with multi-directional invasion, while the viscous fingering with unidirectional invasion was more susceptible occurred in the region near the outlet. Furthermore, increasing invasive viscosity or decreasing invasive velocity and interfacial tension promoted the extension of viscous fingering from the outlet to the inlet, presenting that the subsequent invasive fluid flows toward the outlet. In the case of invasive trunk along a unidirectional path, the invasive flow increased exponentially closer to the outlet, resulting in a significant decrease in the width of the invasive interface. Our work holds promising applications for optimizing invasive patterns in heterogeneous porous media.

© 2024 The Authors. Publishing services by Elsevier B.V. on behalf of KeAi Communications Co. Ltd. This is an open access article under the CC BY-NC-ND license (http://creativecommons.org/licenses/by-nc-nd/

# 4.0/).

# 1. Introduction

The characteristics of immiscible two-phase unstable flow in porous media are of great significance for many earth development behavior, such as geological CO<sub>2</sub> sequestration (GCS), groundwater protection, enhanced oil—gas recovery (EOR) (Lei and Luo, 2021; Nand et al., 2022; Krevor et al., 2023). When invasive fluid with low viscosity displaces defensive fluid with great viscosity in multiple pores during the process of displacement or imbibition, an interface with continuous fingering morphology may be generated, which is called fingering phenomenon (Lenormand et al., 1988; Wang et al.,

1998). At multiple pores space, the defensive fluid with great viscosity can be easily bypassed by invasive fluid with low viscosity, greatly reducing the sweep efficiency (visualizing and quantifying the crossover from capillary fingering to viscous fingering in porous media) (Ferrari et al., 2015; Tang et al., 2020). At a single pore space, the perturbation of invasive interface reduces the replacement efficiency of defensive fluid (Yang et al., 2019). In particular, the influence of fingering phenomenon is greater under the condition of large difference in flow capacity (Bikkina et al., 2016). For instance, when brine flooding is used in the development of heavy oil, the extraction area is severely inhibited by the fingering from synergistic influence of viscosity and wettability (Sorbie et al., 2020; Wang C. et al., 2021). When CO<sub>2</sub> is stored in brine layer, the extremely loose invasive path generated by the difference of viscosity and density makes the presence of gas in a small region (Kim

<sup>\*</sup> Corresponding author. State Key Laboratory of Petroleum Resources and Engineering, China University of Petroleum, Beijing, 102249, China. E-mail address: e1314788@u.nus.edu (Y. Li).

Nomen	clature	$ u_{ m p}$	Variation efficiency of pore size
		$V_{\rm in-de}$	Viscosity ratio
Α	Degree of light absorption of the fluid	w	Invasive width, m
Ca	Capillary number	$w_{ m tr}$	Width of invasive trunk, m
$E_{S}$	Sweep efficiency	X	Phase variable
g	Gravitational acceleration, m/s <sup>2</sup>	$X_{ m f}$	Dimensionless invasive distance
$G_{\mathbf{k}}$	Gini efficiency of invasive width	α	Horizontal angle of the model, $^\circ$
I	Transmitted light intensity	χ	Mobility tuning parameter
K	Permeability, D	Φ	Velocity potential energy
$K_{rw}$	Relative permeability of wetting fluid	$\phi$	Porosity
$K_{rnw}$	Relative permeability of non-wetting fluid	δ	Burst length of invasive interface
M	Mobility ratio	$\eta$	Mutation ratio of invasive interface
$P_{\rm in}$	Pressure of inlet, MPa	$\eta$	Mobility of fluid
$P_{\text{ou}}$	Pressure of outlet, MPa	$\mu$	Viscosity of fluid, mPa s
$r_{ m D}$	Dimensionless radius of invasive interface, m	ho	Density of fluid, kg/m <sup>3</sup>
$r_{ m f}$	Radius of invasive interface, m	$\sigma$	Interfacial tension, mN/m
$\nu_{\rm i}$	Invasive velocity, m/s	au	Invasive time, s

et al., 2019; Singh et al., 2019; Wang S. et al., 2021). A solid understanding of interfacial sensitivity, invasive pathways, and remaining saturation are of crucial to estimate the displacement efficiency and sweep efficiency on multi-phase flow in porous media.

The immiscible two-phase fluid has a tendency of interface instability under the influence of the imbalance among the capillary force, the viscous force and gravity, as depicted in capillary number, mobility ratio and bond number (Aryana and Kovscek, 2012). As the interface instability is interfered by various factors involved in fluid-fluid and fluid-rock interfaces, it is a great challenge to quantitatively study these factors (Hu et al., 2020; Mejia et al., 2021). Additionally, the irregularly shaped and thin interface in multiple pores requires high observation accuracy. Thus, the requirement for an accurate representation of the invasive process and quantified performance of unstable flow in porous media necessitates selecting the experimental model for studying the fingering phenomenon that employs a device with high controllability and pore-scale visualization (Zhao and Mohanty, 2019: Bruns and Babadagli, 2020), Pore-scale experimental models are divided into indirect observation method and direct observation method as shown in Table 1 (Wang et al., 2022; Li et al., 2023). The former utilizes computerized tomography (CT) or nuclear magnetic resonance (NMR) technology to investigate the twophase fluid distribution based on core models, obfuscating the position and shape of the invasive interface (Liu and Mostaghimi, 2017; Patmonoaji et al., 2021; Zhang Y. et al., 2023). The latter employs a highly transparent model, such as microfluidic model, cast thin model, and Hele-Shaw sand-packed model, using a microscopic camera device for directly observation. Furthermore, the microfluidic and Hele-Shaw sand-packed models can provide feedback on the immiscible two-phase flowing in the porous media with controlled pore structure (Blunt et al., 2002).

Based on the displacement experiments of the Hele—Shaw model, the early researchers discussed the modes that determine the branch structures of the interface from the perspective of mathematics and some evaluation parameters. When gravity is ignored, the competition between capillary force and viscous force determines the change of unstable invasive morphology and mode: capillary fingering, viscous fingering, and capillary-viscous cross fingering (McDougall and Sorbie, 1993; Zheng et al., 2017; Huang et al., 2021). Two dimensionless parameters of capillary number and viscosity ratio (*Ca*, *V*<sub>in-de</sub>) are introduced to evaluate the viscous

force, as a driving force, and capillary force, as a resistance (Chen et al., 2017; An et al., 2020). After plenty of microfluidic models and numerical simulation, a phase diagram of invasive pattern based on the capillary number and viscosity ratio was proposed. Except the phase diagram, many experts proposed various methods to capture unstable behavior by flow regimes and general formulations. Hassanizadeh and Gray (1993) and Barenblatt et al. (2003) utilized capillary pressure to predict the evolution of unstable flow. The former adopted thermodynamic approach to define capillary pressure as a basic hysteresis function of saturation at the invasive interfaces. And the latter accounted for nonequilibrium two-phase flow to enhance and broaden the mathematical model in displacement and imbibition processes. Wang Y. et al. (2019) took quasi-stable flow consideration into the unstable flow based on Darcy's law and accurately predict the stable or unstable displacement.

During the immiscible two-phase unstable flow, increasing capillary number can accelerate the morphology of the invasive interface transition from capillary fingering with multi-directional invasion to viscous fingering with unidirectional invasion. Under different displacement modes of fingering, especially in the crossover region where the two invasive patterns, the saturation of the defensive fluid is still large (Cottin et al., 2010; Patmonoaji et al., 2020). The disturbance of flow capacity occurring in the crossover region of capillary and viscous fingering brings challenges to the description of the macroscopic sweep and microscopic displacement efficiency. In the crossover region, the change of the invasive path and the interference to permeability impact the strategies for GCS or EOR under the great difference in the invasive and defensive fluid (Tabrizinejadas et al., 2023).

Pore structure induces the alteration in the connectivity of flowable space, promoting evolution of invasive patterns (Holtzman, 2016). Previous studies have employed the numerical simulation by Navier-Stokes equations, volume of fluid method, lattice Boltzmann simulation, and color-gradient lattice Boltzmann method to track the two-phase interface and evaluate various parameters in the different invasive patterns based on the porous media scenarios (Zakirov and Khramchenkov, 2020; Shi et al., 2021; Zhang H. et al., 2023). In addition, the topological disorder and varying wettability reveal the detail mechanism of capillary force in porous media when fingering phenomenon occurs (Cui et al., 2019; Wei et al., 2022). A power-law relationship between the length of burst of the invasive interface and the saturation of the invasive

**Table 1**Adaptable comparison of pore scale model for fingering research.

Model type	Pore		Interfacial accuracy	Observation method	Model image	
	Authenticity	Controllability				
Core	Strong	Weak	Weak	NMR or CT		
Cast thin	Moderate	Moderate	Moderate	Microscopic device		
Microfluidic/Hele-Shaw	Weak	Strong	Strong	Macro and micro device		

fluid was proposed, accounting for geometry. This relation can be predicted the capillary index, unifying the effects of topological disorder and wettability (Wang Z. et al., 2019).

Despite the capillary number and viscosity ratio establish criteria for judging the fingering pattern in the Hele-Shaw model or the 3D numerical network model, these results, relying on the ideal fluids flow in these models with typical pore structures, raise reasonable questions about their general applicability as criteria for fingering modes (Brandão et al., 2018; Chen et al., 2018; Salmo et al., 2022). The natural rocks with the strong anisotropy at various scale and the alternation of pore-throats easily and commonly induce drastic changes in the morphology of the invasive interface (Keable et al., 2022). In addition, in case of heavy oil development, the invasive fluid frequently employs steam or surfactant solution, resulting in dynamic changes in the viscosity ratio or interfacial tension (IFT) (Bischofberger et al., 2014; Yang et al., 2022). When the IFT decreases to an extreme of 0, immiscible flow becomes more predictable and follows the results from perturbation theory (Riaz and Tchelepi, 2004). There was competition between nonlinearity-driven instability, influence by viscosity ratio and capillary number, and heterogeneity-driven instability possibly associated with pore structures (Furtado and Pereira, 2003). Hence, it holds more significance to investigate diverse fluids with various viscosities and IFT in the heterogeneous flow space.

In this paper, to investigate the evolution performance of invasive patterns, invasive velocities, viscosity, and variation of pore size were systematically changed in the homogeneous pore structures (Chang et al., 2020). Visual experiments permitted real-time imaging of the invasive processes at the pore scale, facilitating the quantification of the invasive morphology and the fluid occupancy saturation in local apertures (Zhao et al., 2023). Subsequently, laminar two-phase flow numerical simulation was established by employing the finite element method (FEM) to calculate immiscible two-phase flow. Through a series of capillary numbers by adjusting three parameters, we studied the evolution boundaries of invasive patterns and extended the classic phase diagram in the limits of displacement. Building upon experimental results and velocity potential equations, the invasive branches stemming from fingering gradually merged with the invasive trunk, leading to the suppression of lateral expansion.

Consequently, there is an increased burst distance of the invasive interface, a phenomenon corroborated in the mathematical model. This work, for the first time, introduces a framework for sweep efficiency in the pore-throat alternate model, where three parameters were adjusted to achieve a constant capillary number. It enhances our understanding of which parameters are more likely to contribute to GCS or EOR.

## 2. Methodology

# 2.1. Experimental observation

#### 2.1.1. Experimental materials

The work chosen for fingering phenomenon employed the microfluidic models and the Hele—Shaw sand-filled models, which both visually depicted the fluid distribution at the macro and micro scale. The microfluidic model features flow channels ranging from 35 to 350  $\mu m$ , while the Hele—Shaw sand-packed models had flow channels within the range of 25–250  $\mu m$ . A comparison of their respective advantages, disadvantages, and the primary research emphases in the work can be presented as Table 2.

Owing to accurate pore structures and strong pore structure stability, microfluidic models emphasize the study of pore heterogeneity and special capillary number with different injection velocities and viscosities. In contrast, the Hele—Shaw model predominantly examines the influence of various fluid on the performance of the fingering phenomenon.

Defensive fluids: The defensive fluids originally existing in the models were oil and brine. The salinity of brine was measured at  $2.86 \times 10^4$  mg/L as shown in Table 3. The viscosity of oil used in the microfluidic model was 10 mPa s at experimental condition. And the viscosity and density (degassed) of oil applied in the Hele—Shaw model were 100 mPa s and 0.87 g/cm<sup>3</sup> at 55 °C.

Invasive fluids: In the microfluidic models, the invasive fluids differed only in viscosity. The solvent was the brine, while the solute was non-ionic polyacrylamide (HPAM) with a molecular weight of 15 million. The viscosity of invasive fluid was adjusted by the proportion of the solute in the solution.

In the Hele—Shaw sand-packed models, the choice of invasive fluids needed to consider the IFT and viscosity. The low-viscosity solution with half the viscosity of the oil-phase defensive fluid, and steam with reducing the viscosity of the oil-phase defensive fluid were employed to verify the influence of viscosity on fingering. The surfactant solution was composed of sodium oleate (SO) and cetyl trimethyl ammonium chloride (CATB) in a ratio of 1:1. The spinning drop tensiometer (SVT20N) indicated an oil—water IFT of 0.3 mN/m (Pratama and Babadagli, 2020). Besides, the apparent viscosity of the emulsion by mixing the surfactant solution with oil-phase defensive fluid was seriously affected by the oil—water ratio. The viscosity of the emulsion, increasing with the oil—water ratio, was significantly greater than that of brine but lower than that of oil-phase defensive fluid.

# 2.1.2. Microfluidic models

The microfluidic models were conducted to observe the

**Table 2**The advantages and disadvantages of experimental models.

Model type	Advantages	Disadvantages
Microfluidic	High reusability.     Accurate pore structure.     Strong pore structure stability.	1. Incorporating clay minerals and other interstitial materials into the reservoir presents difficulty.  2. Greater viscosity fluids are difficult to inject.
Hele—Shaw sand-packed	<ol> <li>Strong injectivity.</li> <li>Filling a variety of interstitial materials.</li> </ol>	Too idealized pore structure.     Rock is indistinguishable from fluid.

**Table 3** The salinity and composition of brine.

Type of ions	Na <sup>+</sup>	${\rm Mg}^{2+}$	$Ca^{2+}$	$CO_3^{2-}$	HCO <sub>3</sub>	Cl <sup>-</sup>	$\mathrm{SO}_4^{2-}$	Total
Concentration of ions, mg/L	9121	152.2	320.2	2726.2	11606.4	4452.6	250.8	28629.4

fingering pattern by various parameters of capillary number in the heterogeneous pore structure. The work introduces the pore variation efficiency for a quantitative assessment of pore heterogeneity, expressing as

$$V_{\rm p} = \frac{\sqrt{\sum_{i=1}^{N} (r_i - \overline{r})}}{\overline{r}} \tag{1}$$

where  $V_{\rm p}$  represents the variation efficiency of pore size;  $r_i$  represents the radius of each pore; and  $\overline{r}$  represents the average radius of pores. The anisotropy of the microfluidic model intensifies with an increasing variation efficiency of pore size. Through cast thin from cores, various images displaying the pore structure and the heterogeneous property from small to large can be shown in Fig. 1.

The microfluidic models, made by Norland Optical Adhesive (NOA81), were neutrally wetting by a UV exposure time of 20 s. Detailed model parameters can be presented in Table 4. The permeability and porosity differences among these microfluidic models were minimal, yet there was a noticeable variance in porethroat width, aligning with our experimental design specifications.

Based on the pore template from cast thin, microfluidic models were manufactured with hydrophilic pores. The size of the visualization region of the microfluidic model was 5 cm  $\times$  2.5 cm. In addition, grooves were etched on both the inlet and outlet ports of the upper plate in the foundational model to ensure the consistent progression of the injected fluid. The microfluidic model was placed in the visualization system to carry out displacement experiment and image acquisition. The experimental apparatus contained a fluid-supply system, an image-acquisition system, and a fluid-collection system as shown in Fig. 2.

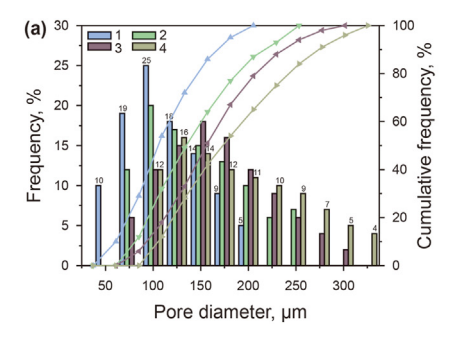
The detailed experiment is as follows.

- (1) The microfluidic model was evacuated for 2 h. Then, the brine was injected into the model by the pump at a flow velocity of 0.1  $\mu$ L/min until the brine can flow steadily from the outlet and the pore volume of the microfluidic was calculated by the weighing method.
- (2) Maintaining the inlet pressure at 1000 bar with MFXS-EZ, the oil-phase defensive fluid was injected into the microfluidic model until it consistently flowed from the outlet. Then, the model was heated to 50 °C for more than 72 h.
- (3) According to the various scenarios studied for the capillary number, invasive fluids were injected into the model at different injection velocities.

The visualization experiment on microfluidic model was conducted to obtain images of fingering performance at various scenarios. The sweep efficiency was calculated by analyzing the distribution of invasive and defensive fluids.

The detailed sweep efficiency procedures are presented as follows.

- The saturated brine image was used as the base background image by binarization. Then, the work can get the rock skeleton.
- (2) The base background image after displacement process was binarized again to distinguish the oil and brine.
- (3) A second comparative analysis is required for the oil—water boundary. Pixels with edges washed by brine but still containing remaining oil are categorized as swept region.
- (4) The proportion of brine in the total sum of oil and brine was computed to assess sweep efficiency, which was expressed as



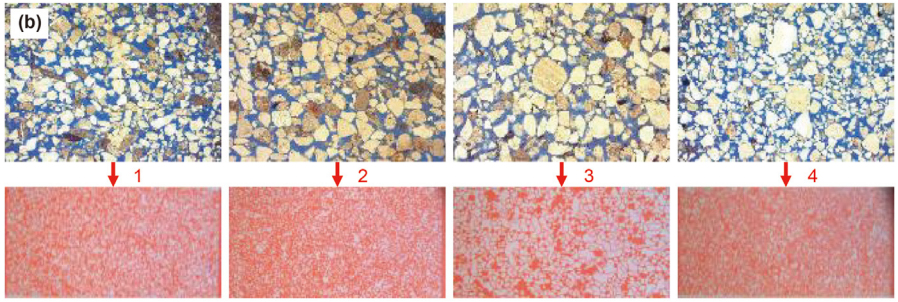


Fig. 1. The distribution of pore radius in the microfluidic models.

**Table 4**Basic parameters of microfluidic models.

Model No.	Average pore diameter, μm	Average throat width, μm	Porosity, %	Permeability, mD	Coefficient of heterogeneity
1	92.62	5.84	30.60	2930	15.27
2	106.41	6.06	28.80	2600	24.79
3	125.04	8.16	29.70	3110	32.32
4	154.69	11.47	26.50	2580	62.62

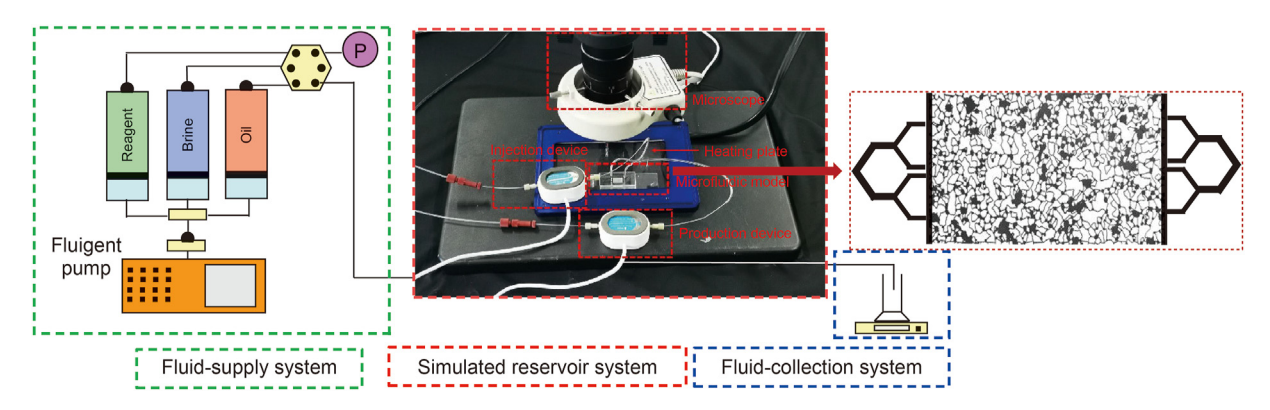


Fig. 2. The schematic diagram of experimental apparatus employing microfluidic model.

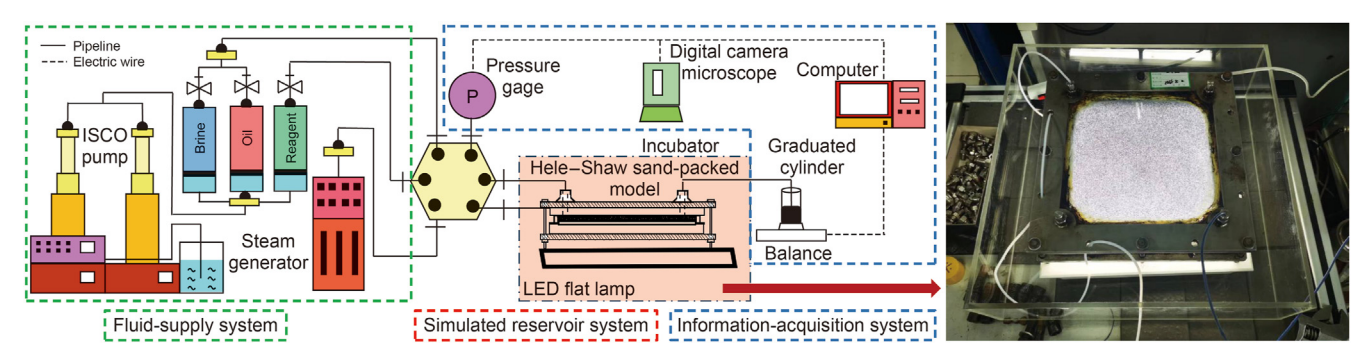


Fig. 3. The schematic diagram of experimental apparatus employing Hele-Shaw model.

$$E_{\rm S} = \frac{PX(\rm o)}{PX(\rm o) + PX(\rm b)} \times 100\% \tag{2}$$

where PX(o) represents the pixels occupied by oil; PX(b) represents the pixels occupied by brine.

#### 2.1.3. Hele-Shaw models

The Hele—Shaw sand-packed models were conducted to observe the fingering pattern affected by various fluids. Keeping the injection velocity constant led to variations in the capillary number. The Hele—Shaw sand-packed model consisted of two glass plates with a length of 25 cm (Wu et al., 2019) and one of the glass plates was equipped with four penetrating holes to simulate the wellbores. In addition, the model comprised machine parts represented by glass beads, simulating the rock skeleton, and thermal-resistant colloids, simulating formation cement. The glass beads were evenly packed in the Hele—Shaw sand-packed model, measuring the porosity by volume method. And the permeability of the Hele—Shaw sand-packed model has estimated the intrinsic permeability by the rhomboidal structure diameter as following equation (Pratama and Babadagli, 2020):

$$K = \frac{d_{\rm m}^2}{180} \cdot \frac{\phi^3}{\left(1 - \phi^2\right)} \tag{3}$$

where  $d_{\rm m}$  represents the size of glass beads; and  $\phi$  is the porosity of the Hele—Shaw sand-packed model. The models were filled with glass beads of 60 mesh (250  $\mu$ m), which indicates that the maximum size of pores was less than 250  $\mu$ m.

The experimental apparatus was divided into three systems as shown in Fig. 3: a fluid-supply system, a simulated reservoir system, and an information-acquisition system. The fluid-supply systems used by the Hele–Shaw model and the microfluidic model were similar. And the information acquisition system contained a digital camera microscope and a full HD camera. The digital camera microscope, manufactured by the Swedish Optilia, can achieve up to  $200\times$  magnification in the visible spectrum for capturing microscopic images.

The detailed experimental procedure is as follows.

(1) Establishment of simulated oil reservoir. Inject the brine into the model by the pump at an injection velocity of 0.2 mL/min until the brine can flow steadily from the outlet and calculate

the pore volume of the Hele—Shaw model by the weighing method.

- (2) Inject the heavy oil into the model at an injection velocity of 0.1 mL/min until the heavy oil can flow steadily from the outlet. Then, the model is heated to 50 °C for more than 72 h.
- (3) According to the various scenarios studied from the capillary number, various fluids follow a predetermined sequence at a constant injection velocity of 0.2 mL/min.

The macroscopic images could be processed by the standard oil saturation with light transmission measurement and the grid segmentation method based on the Beer–Lambert equation can be quantified as follows (Chen et al., 2017):

$$I = I_{oi}e^{-AS_o} \tag{4}$$

where I represents the transmitted light intensity; A represents the degree of light absorption of the fluid;  $I_{\rm oi}$  represents the initial intensity of the transmitted light in oil-saturated model. The calibrated saturation values from individual grids were amalgamated to create the oil saturation diagram.

#### 2.2. Numerical simulation

#### 2.2.1. Model construction

In the work, a computational fluid dynamic (CFD) with commercial numerical software (COMSOL Multiphysics) was used to present the establishment of simulation model for fingering phenomenon in heterogenous pore space. For a quantitative investigation of the fingering phenomenon, a 2D model with small size (20 mm  $\times$  10 mm) was employed, aligning with the characteristics of the experimental models detailed in the former section, as illustrated in Fig. 4.

Geological conditions: In the representation, the grains were depicted using an equilateral triangular array of circles. Specially, the bulk grain diameter was set to 500  $\mu$ m, while the pore throat diameter was set to 250  $\mu$ m. Grain surfaces were designated as hydrophilic with a certain contact angle. To facilitate fluid ingress into the model, an inlet was positioned in the lower left corner.

Initial conditions: The initial temperature and pressure of the simulation model refer to these conditions of the experiments. The inlet boundary condition was set to a constant current injection velocity, while the outlet boundary condition was a constant production pressure. The simulation used the Navier—Stokes equations

to express the momentum transport, including the IFT and conservation of mass. At the initial moment, the entire interior of the model was saturated with oil.

Pore grids: The COMSOL software was used to simulate the proposed model of immiscible two-phase flow process in heterogeneous pores (Hu et al., 2018). The flow spacing of rock particle in this study was uniform, meaning that the interconnected pores and throats alternate equally throughout the model. Considering the inaccurate meshing result in insufficiently calculated capillary forces to propel the invasive fluid, a triangular mesh was employed in the inner region and a hyperfine tetragonal mesh was designed in the boundary region.

#### 2.2.2. Mathematical expression

The simulation model for studying the fingering phenomenon encompassed two physical fields and was constructed on the following assumptions.

- Water and oil existed in the reservoir pore obey the low of Darcy.
- The model does not involve the influence of gravity.
- No mass flux occurs between the rock grain surface and the non-inlet/outlet boundary, and all surfaces have same contact angle and no fluid slippage.
- During the displacement process, oil and water are incompressible fluids.

The governing equations of the model was described to the transport of mass and momentum between oil and water based on Navier—Stokes equations, as follows:

$$\frac{\partial(\rho_{i}u_{i})}{\partial t} + \rho(u_{i} \cdot \nabla)u_{i} = \nabla\left[-\rho_{i}I + \eta\left(\nabla u_{i} + (\nabla u_{i})^{\mathsf{T}}\right)\right] + F + \rho_{i}g$$
 (5)

Simultaneously, simulating the fingering phenomenon should emphasize the interfacial two-phase flow via the phase field method, which requires the control of the two-phase interface, as follows:

$$\frac{\partial x_i}{\partial t} + \nabla \cdot (ux_i) = \nabla \cdot \frac{\gamma \lambda}{\varepsilon_{\rm pf}^2} \nabla \psi \tag{6}$$

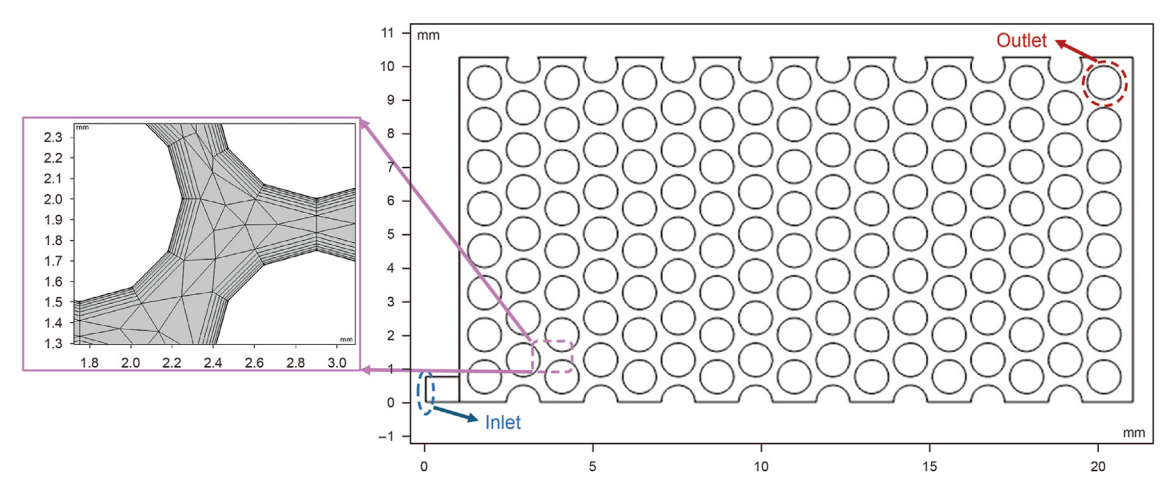


Fig. 4. The numerical model of fingering phenomenon in heterogenous pore space.

$$\begin{cases} \psi = -\nabla \cdot \varepsilon_{\rm pf}^2 \nabla x + \left(x^2 - 1\right) x + \frac{\varepsilon_{\rm pf}^2}{\lambda} \cdot \frac{\partial f}{\partial x} \\ \lambda = \frac{3\varepsilon_{\rm pf} \sigma}{\sqrt{8}} \\ \gamma = \chi \varepsilon_{\rm pf}^2 \end{cases}$$
(7)

where  $\varepsilon_{\rm pf}$  represents the parameter for controlling the interface thickness; x represents the phase variable;  $\sigma$  represents the surface tension;  $\chi$  represents the mobility tuning parameter.

#### 2.2.3. Model validation

Before employing the phase-filed method to simulate the twophase flow in porous media, we verify its suitability for representing immiscible two-phase flow. This verification involves conducting a classic layered two-phase flow test.

On the setting of boundary conditions, the validated model has a total thickness of 200  $\mu m$  and comprises three distinct regions. The region near the outer boundary is filled with wetting fluid, while the central region is filled with non-wetting fluid. The width ratio of various regions determines the saturation of two-phase fluids as shown in Fig. 5.

On the validation with analytical solutions, the theoretical method applied in relative permeability of two-phase flow can be expressed as follows (Fei et al., 2023):

$$\begin{cases} k_{\Gamma,W} = \frac{S_W^2(3 - S_W)}{2} \\ k_{\Gamma,NW} = S_{NW} \left[ \frac{3}{2} M + S_{NW}^2 \left( 1 - \frac{3}{2} M \right) \right] \end{cases}$$
 (8)

where  $k_{\rm rw}$  and  $k_{\rm rnw}$  represent the relative permeability of wetting and non-wetting fluids, respectively; M represents the mobility ratio. According to Darcy's law, the relative permeability can be calculated by the flow rate of various fluids at the outlet.

As shown in Fig. 6, the results of relative permeability from the simulated model and analytical solutions perform good agreement. When the mobility ratio is less than 1, the sum of the two-phase relative permeability does not exceed 1. Conversely, when the mobility ratio is greater than 1, the sum of the two-phase relative permeability exceeds 1, presenting the "lubrication".

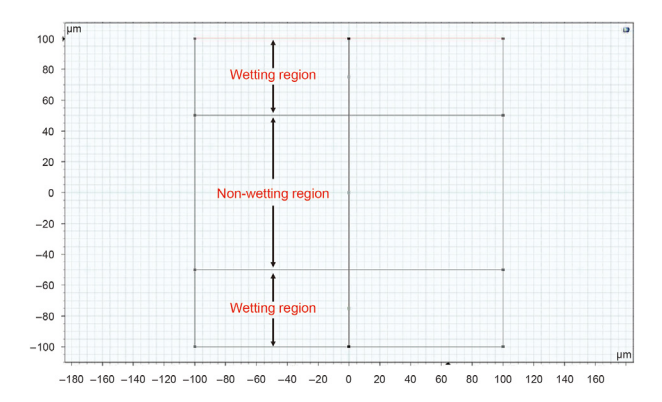
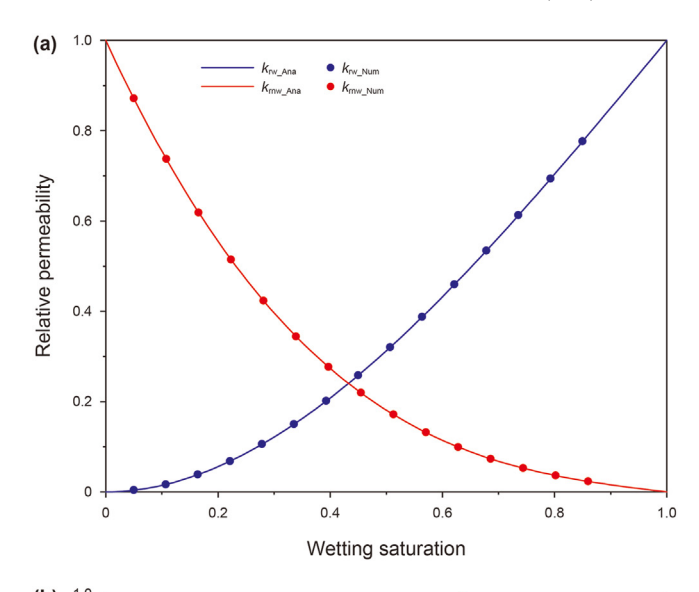
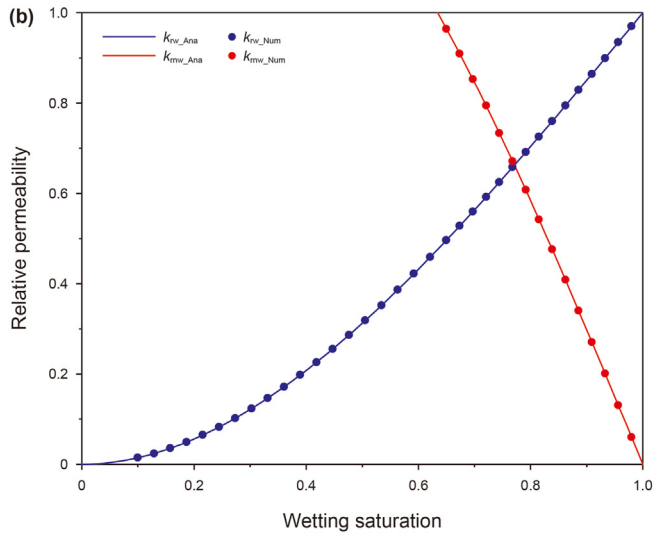
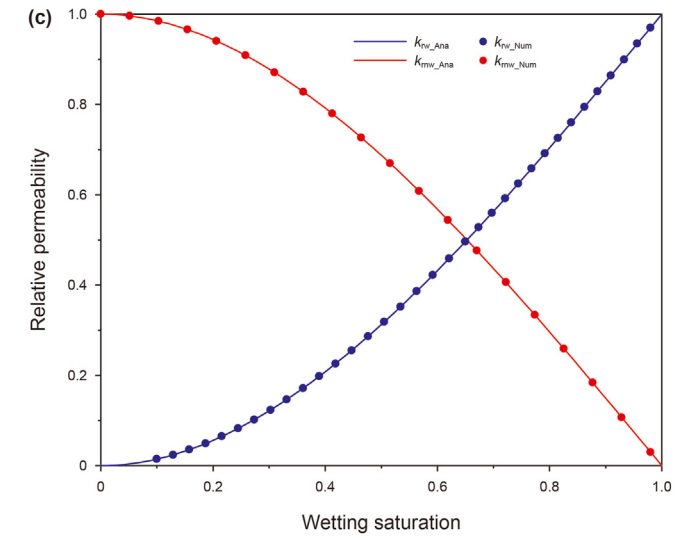


Fig. 5. Geometric diagram of the validated model.







**Fig. 6.** Comparison of analytical solutions and numerical model on relative permeability. (a) M = 0.1; (b) M = 1; (c) M = 2.



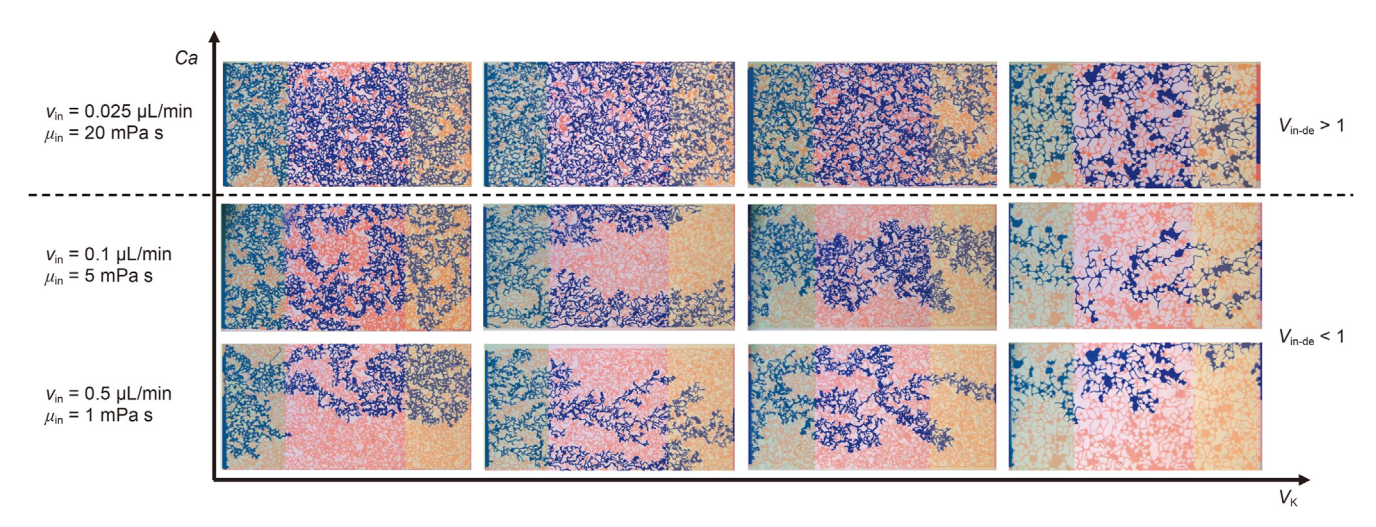


Fig. 7. Distribution diagram of two-phase fluids based on microfluidic models.

#### 3. Results and discussion

#### 3.1. Analysis of microfluidic model

Keeping the interfacial intension constant, the experiments based on microfluidic models manipulated the capillary number by adjusting injection velocity and viscosity ratio of invasive-defensive fluid in the microfluidic models. To facilitate the description of the fingering phenomenon, the region with 20% model length along the injection direction near the inlet boundary was designated as the region near the inlet (greenish region). Similarly, the region with 20% model length against the injection direction near the outlet boundary was designated as region near the outlet (yellowish region) as shown in Fig. 7.

When the viscosity ratio ( $V_{\rm in-de}$ ) surpassed 1, a stable invasive pattern gradually spread from the region near the inlet to the region near the outlet. Under the stable invasive pattern, the sweep efficiency surpassed 85% in all microfluidic models, indicating that the anisotropy of pore structure has little effect on the stable invasive pattern.

When the viscosity ratio failed to exceed 1, the invasive interface cannot maintain the stable invasive pattern. In case of the identical capillary number, the injection velocity was heightened, while the invasive viscosity was decreased in following scenarios. Under the condition of great viscosity and low injection velocity, conspicuous lateral expansion occurred, leading to an insignificant distinction between the invasive trunk and invasive branch. As the anisotropy of the pore structure increased, the extension distance of the invasive branch shortened, resulting in a gradual shift from multi-directional invasion to unidirectional invasion. Under the condition of low viscosity and great injection velocity, shorter burst distance generated by lateral expansion signified the characteristics of unidirectional invading. As the anisotropy of the pore structure

increased, the angle between the invasive trunk and branch also gradually reduced, resulting in the narrow width of the invasive trunk.

In scenarios with great sweep efficiency, the initially unstable invasive interface, predominantly governed by capillary fingering with lateral expansion, undergoes notable changes. As the invasive interface extends further, the cumulative impact of capillary dissipation, reducing displacement energy of the invasive fluid, results in reduced length and diminished occurrence of invasive branches. The morphology of the invasive interface undergone a transformation, shifting from a multi-directional invasive pattern as capillary fingering to a unidirectional invasion pattern as viscous fingering. The distinctive angle between the trunk and branches plays a decisive role in determining the sweep efficiency in the crossover region characterized by capillary-viscous fingering.

When the invasive viscosity was reduced and invasive velocity was increased, the unstable invasive interface caused by capillary fingering with multi-directional invasion gradually transformed to that controlled by viscous fingering with unidirectional invasion. The invasive interface controlled by viscous fingering was manifested in the reduction of the angle between the invasive trunk and the invasive branches, as well as lateral expansion ceased after passing through the region near the inlet, giving rise to a distinct narrow invasive interface dominated by viscous fingering and the significant reduction of the sweep efficiency. Image processing method of microfluidic model was employed to calculate the sweep efficiency. Displacement efficiency was derived from oil recovery divided by sweep efficiency, evaluating the decreasing performance of oil saturation in the swept region as shown in Table 5.

In terms of sweep efficiency, the heterogeneity of pore-throat structure has great influence on the development performance from microfluidic experiments. Compared the injection velocity, the great viscosity of invasive fluid has an improved performance in

**Table 5**The performance of unstable invasive interface based on microfluidic.

Model No.	Sweep efficiency, %			Displacement efficiency, %		
	$ u = 0.5  \mu \text{L/mim} $ $ \mu = 1  \text{mPa s} $	$ u = 0.1 \ \mu \text{L/mim} $ $ \mu = 5 \ \text{mPa s} $	$ u = 0.025 \ \mu \text{L/mim} $ $ \mu = 20 \ \text{mPa s} $	$ u = 0.5 \ \mu \text{L/mim} $ $ \mu = 1 \ \text{mPa s} $	$ u = 0.1 \ \mu \text{L/mim} $ $ \mu = 5 \ \text{mPa s} $	$ u = 0.025 \ \mu \text{L/mim} $ $ \mu = 20 \ \text{mPa s} $
1	47.7	64.2	91.4	56.3	62.8	71.5
2	35.8	58.4	93.6	58.5	64.1	70.8
3	31.5	41.5	92.1	55.6	65.5	72.4
4	19.2	23.7	88.5	53.5	62.4	70.6

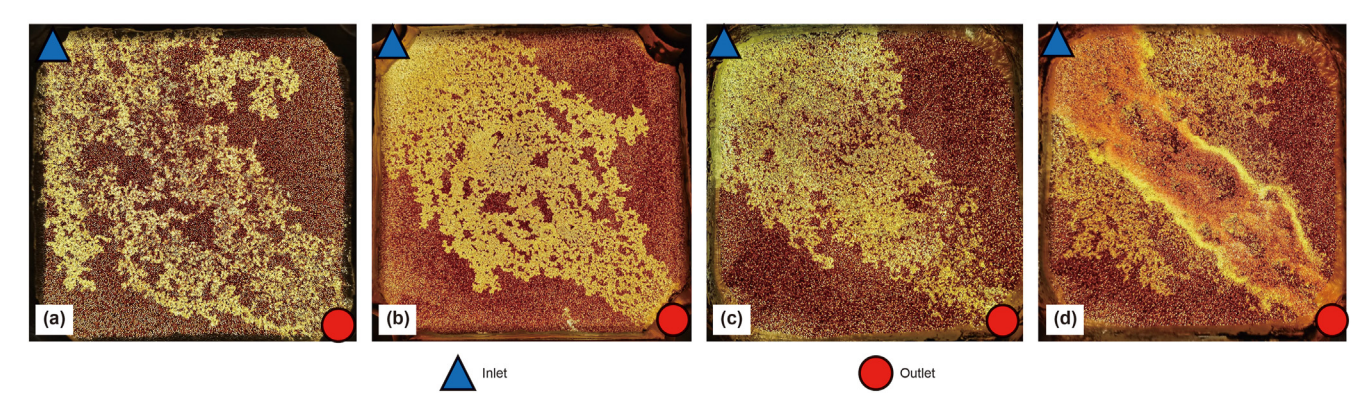


Fig. 8. Two-phase fluid distribution diagram of fingering based on Hele—Shaw sand-packed model. (a) Steam flooding; (b) Brine flooding; (c) Low-viscosity fluid flooding; (d) Subsequent surfactant flooding.

the sweep efficiency under constant capillary number. In terms of displacement efficiency, the heterogeneity of pore-throat structure has small influence on the development performance. Similarly, the improvement of development performance in invasive viscosity was better than that of velocity. Furthermore, the viscosity improvement of displacement efficiency was evidently lower than that of sweep efficiency.

Primarily, it is obvious that both the capillary number parameter and the heterogeneity of the flow space notably influence the sweep efficiency, whereas only the capillary number alone exerts a relatively minor impact on displacement efficiency.

#### 3.2. Analysis of Hele-Shaw model

Keeping the pore structure and defensive fluid unchanged, the displacement experiments based on Hele—Shaw sand-packed models manipulated the capillary number by adjusting the type of invasive fluid. Fully leverage the Hele—Shaw model characteristics of facilitating injection, the pores were saturated with defensive fluid with heavy oil. The high repeatability and isotropy of pore structures minimize the impact of pore structure, allowing for a concentrated exploration of the influence of fluid type on the invasive patterns.

#### 3.2.1. Morphology of invasive interfaces

From the aspect of invasive morphology, in scenario a, the injection of high-temperature steam caused the viscosity difference to gradually widen from the inlet to the outlet. As a result, a pronounced lateral expansion of the invasive interface occurred near the inlet as shown in Fig. 8(a). While advancing the invasive interface into the reservoir, the viscosity differences decreased due to heat loss and the displacing power failure caused by capillary dissipation constrained the lateral expansion of the invasive trunk, leading to a narrowing of the invasive interface as it approached the outlet.

In scenario b, the injection of brine with smaller viscosity ratio (0.02) resulted in less lateral expansion compared to steam flooding as shown in Fig. 8(b). With less lateral expansion, the invasive fluid was more concentrated at the shorter invasive interface, resulting in a greater injection velocity in the region near the inlet. Under the support of greater injection velocity, the pronounced backflow effect of invasive fluid made the invasive branches distributed densely. Subsequently, the narrowing invasive interface and fewer branches had the lower displacing power failure, resulting in the strong lateral expansion by the capillary fingering and weakened backflow effect.

In scenario c, the injection of low-viscosity brine with the greater viscosity ratio (0.8) resulted in strong backflow effect in the region near the inlet as shown in Fig. 8(c). The invasive fluid with great viscosity resulted in displacing power failure, leading to the rapid collapse of the lateral expansion and backflow effect in the region near the inlet. The rise in capillary number and viscosity ratio ensured a uniform pressure difference across the invasive interface, leading to an obvious hindrance branch development and a gradual narrowing of the invasive trunk width from the inlet to the outlet.

In scenario d, the injection of reddish surfactant fluid led to the IFT from 30 to  $0.3 \, mN/m$  and a 100-fold rise in the capillary number. After the emulsion existed, sufficient displacement power restarted the lateral expansion pushed emulsion with great flow resistance to both sides of the invasive interface. With the advance of surfactant, the low energy loss generated by great capillary number drove the emulsion to line up stably on both sides of the invasive interface as shown in Fig. 8(d).

Invasive width perpendicular to this direction can be quantified to describe macroscopic swept efficiency. The widths were arranged in descending order, serving as the abscissa, while the corresponding width proportions were plotted as the ordinate. Then, the Lorentz curve and Gini efficiency of width distribution, describing the width change of the invasive interface, can be expressed as

$$\begin{cases} x_{m} = \frac{\sum_{i=1}^{m} w_{i}}{\sum_{i=1}^{n} w_{i}} \\ y_{m} = \frac{\sum_{i=1}^{m} P_{i}}{\sum_{i=1}^{n} P_{i}} \\ G_{k} = \frac{\int_{0}^{1} y_{m} dx_{m}}{\int_{0}^{1} y_{n} dx_{n}} = 2 \int_{0}^{1} y_{m} dx_{m} - 1 \end{cases}$$

$$(9)$$

where  $w_i$  represents the width of the invasive interface filled with invasive fluid;  $P_i$  represents the proportion of different size of width;  $G_k$  represents the Gini efficiency of width distribution. In general, a Gini efficiency below 0.3 signifies a minimal difference in

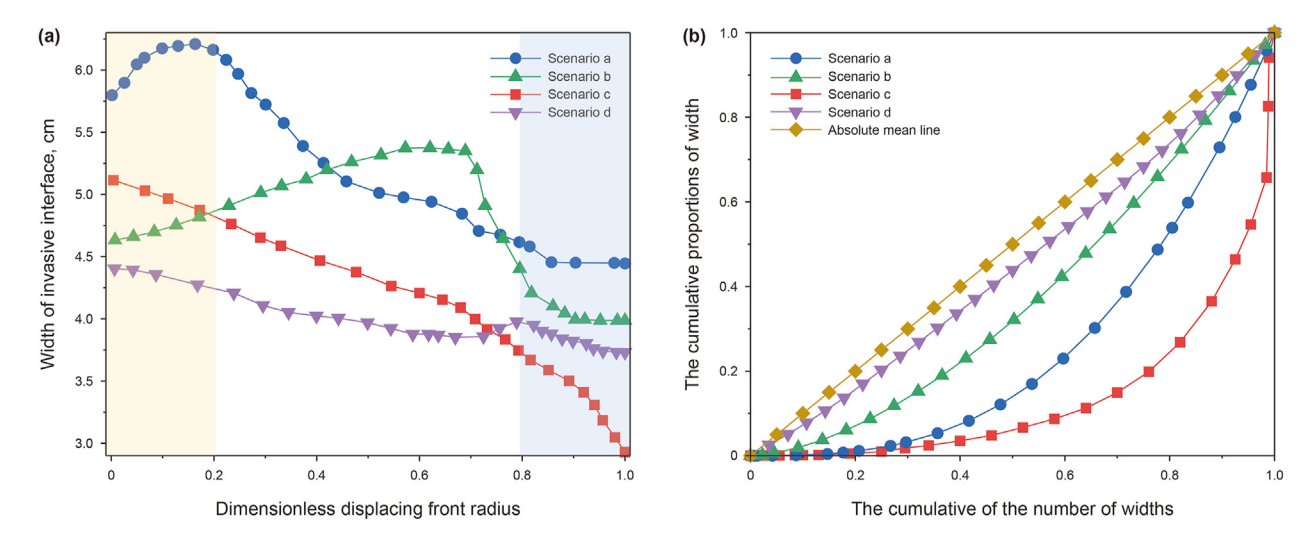


Fig. 9. The Lorentz curve of invasive width based on the Hele-Shaw sand-packed model. (a) Interfacial width along the inlet-outlet line; (b) The Lorentz curve.

width distribution, whereas a Gini efficiency surpassing 0.5 indicates a substantial difference in width distribution.

As shown in Fig. 9, the width difference at the invasive interface is most pronounced as shown in scenario c, whereas it is minimal in the scenario d. Except the scenario d, the viscosity ratio of the other scenarios in order from large to small as:  $V_c > V_a > V_b$ . Simultaneously, the Gini efficiency of width distribution of the first scenarios in order from large to small as:  $G_{kc} > G_{ka} > G_{kb}$ . In terms of viscosity, a lower viscosity of invasive fluid has diminished energy loss in the flow channels, indicating that the invasive energy was more concentrated at the invasive interface so that noticeable lateral expansion can be developed. In terms of the IFT, the surfactant significantly mitigated energy loss in the flow channel. Consequently, a predominant portion of the invasive energy concentrated at the invasive interface, ensuring the stability of invasive width. In brief, the effective transport of invasive energy to the invasive interface is crucial for enhancing the sweep efficiency of lateral expansion.

#### 3.2.2. Saturation affected by invasion

The fingering phenomenon can obviously impact both the sweep efficiency and displacement efficiency. The width of invasive interface can quantitively describe the sweep efficiency. Additionally, the values of oil saturation in various regions also indicate the fingering strength on the terms of displacement efficiency. The surfactant greatly enhances the hydrophilicity of the rock surface,

masking the influence of the fingering phenomenon on microdisplacement efficiency, thereby excluding the consideration of oil saturation affected by the surfactant.

Image processing method of Hele—Shaw sand-packed model was employed to calculate the sweep efficiency and displacement efficiency. The defensive fluid saturation diagram reveals that, in the capillary fingering invasive pattern depicted in Fig. 10(a), the saturation values of the invasive fluid at the toe of the invasive branches exceed those at the heel. Moreover, the saturation difference between the toe and the heel of the invasive branches gradually diminished with the increase in the invasive radius of invasive interface. In addition, the replacement efficiency was also one of the indicators to evaluate the development scenarios, as shown in Table 6. The replacement efficiency was the producing volume of defensive fluid divided by the injecting volume of invasive fluid. According to the development performance, the replacement efficiency had significant growth in the scenario of increasing the invasive viscosity (see Fig. 11).

To quantify regional differences in oil saturation, a constant width was chosen as the sampling strip for oil saturation from the inlet to the outlet. Average oil saturation can directly reflect the displacement efficiency of the invasive fluid. While the minimum oil saturation can present the ability of the invasive fluid to extract the defensive fluid.

After steam flooding (Scenario a), the invasive interface exhibited a marked nonlinear rise in oil saturation. Outside the

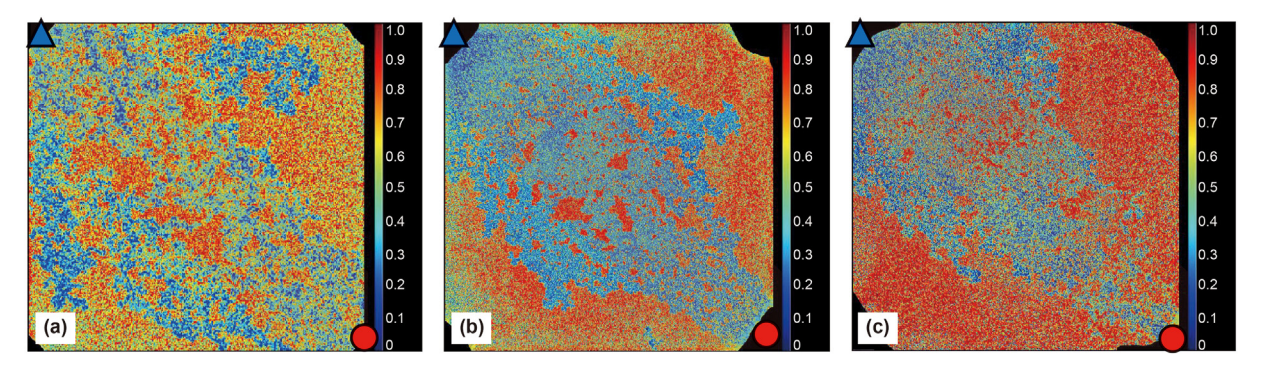


Fig. 10. Diagram of defensive fluid saturation in fingering phenomenon based on Hele—Shaw sand-packed model. (a) Steam flooding; (b) Brine flooding; (c) Low-viscosity brine flooding.



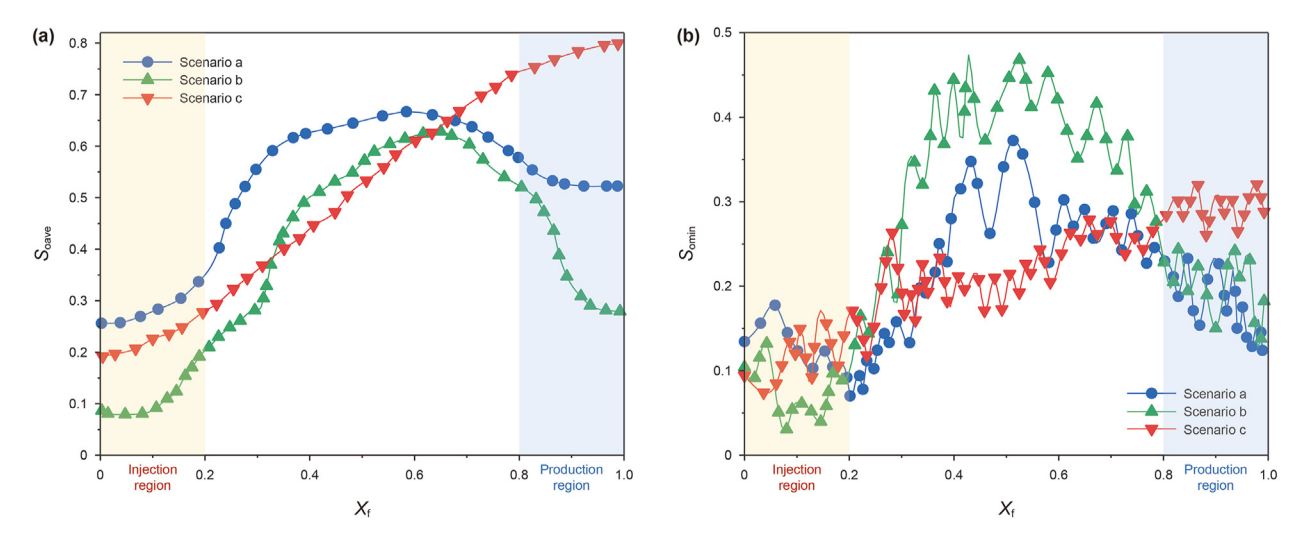


Fig. 11. The oil saturation along the inlet-outlet line based on the Hele-Shaw sand-packed model. (a) Average oil saturation; (b) Minimum oil saturation.

**Table 6**The performance of unstable invasive interface based on Hele—Shaw sand-packed model.

Scenario No.	Oil recovery, %	Sweep efficiency, %	Displacement efficiency, %	Replacement efficiency, %
a	25.4	39.1	65.0	38.5
b	23.2	45.3	51.2	25.9
С	27.6	37.7	73.2	54.0

boundary of the region near the inlet, the average and minimum oil saturation experienced a swift increase. This can be primarily ascribed to the diminished efficacy of viscosity reduction after steam condensation into hot water, resulting in reduced displacement efficiency. In the central region, flaky remaining oil evidently increased the oil saturation. However, shortly thereafter, the flaky remaining oil underwent segmentation and reduction again, causing a minor decrease in oil saturation in the region near the outlet.

After brine flooding (Scenario b), the nonlinear characteristics of the invasive interface diverged from those observed during steam flooding. The vigorous backflow induced by the invasive fluid to strongly extract the defensive fluid, resulting in a low average oil saturation in the region near the inlet. Conversely, the large-sized flaky remaining oil, generated by lateral expansion, dramatically elevated the oil saturation in the central region. However, the oil saturation characteristics were similar for brine flooding and steam flooding in the region near the outlet. A common feature in first both scenarios manifested as the intensified lateral expansion by the invasive fluid, assisted by a pressure drop funnel, resulting in a reduction in oil saturation.

After low-viscosity brine flooding (Scenario c), the oil saturation exhibited a monotonically increasing trend. In essence, the synergistic impact of weak lateral expansion and the gradual amount of flake remaining oil contribute to the increase of oil saturation in a controllable state. Specifically, the amplitude of change in oil saturation is smaller than in the first both scenarios.

#### 3.3. Analysis of numerical model

Based on the analysis of two experimental models, when the viscosity ratio was inferior to 1, the stable invasive pattern broke down, leading to typically lateral flow and reflux phenomena in the region near the inlet, which indicated that capillary fingering with multi-directional invading dominated the invasive process.

However, relying solely on experimental methods to assess the impact of the capillary number on fingering can only delineate trends without providing a mathematical fit. Concurrently, the influence of fingering on sweep efficiency under different capillary number can be displayed. As surfactant molecules, which influence IFT, gradually approach the invasive interface and experience a decrease in surfactant concentration, variations in IFT arise across different regions. Consequently, this leads to inaccuracies in testing the impact of experimental methods on IFT. For a more precise investigation into the influence of fingering on the invasive interface, simulation is employed for verification purposes.

#### 3.3.1. Fingering affected by velocity

In alignment with the microfluidic model results, simulation results also affirm that a greater capillary number affected by injection velocity fosters enhanced pointing sweep efficiency as shown in Fig. 12.

At low injection velocity, the number of lateral branches rarely increase in the invasive interface when the injection velocity had a rise. At high injection velocity, the width of the trunk of the invasive interface was also enlarged, which greatly contributed to the improvement of sweep efficiency as shown in Fig. 12(b). However, the edge of the trunk still exhibited great oil saturation and considerable potential for extraction of defensive fluid. A large increase in the injection velocity can further extend the length and the width of the invasive branch, thus further increasing the sweep efficiency.

#### 3.3.2. Fingering affected by IFT

As shown in Fig. 8(d), the great capillary number contributed by low interfacial intension prevents the new invasive interface, displaying reddish region, from producing more invasive branches. Because the surface also has an effect on rock wettability during invasive experiments, the simulation results can better reflect the uniqueness of the effect of IFT. Furthermore, one can conceptualize

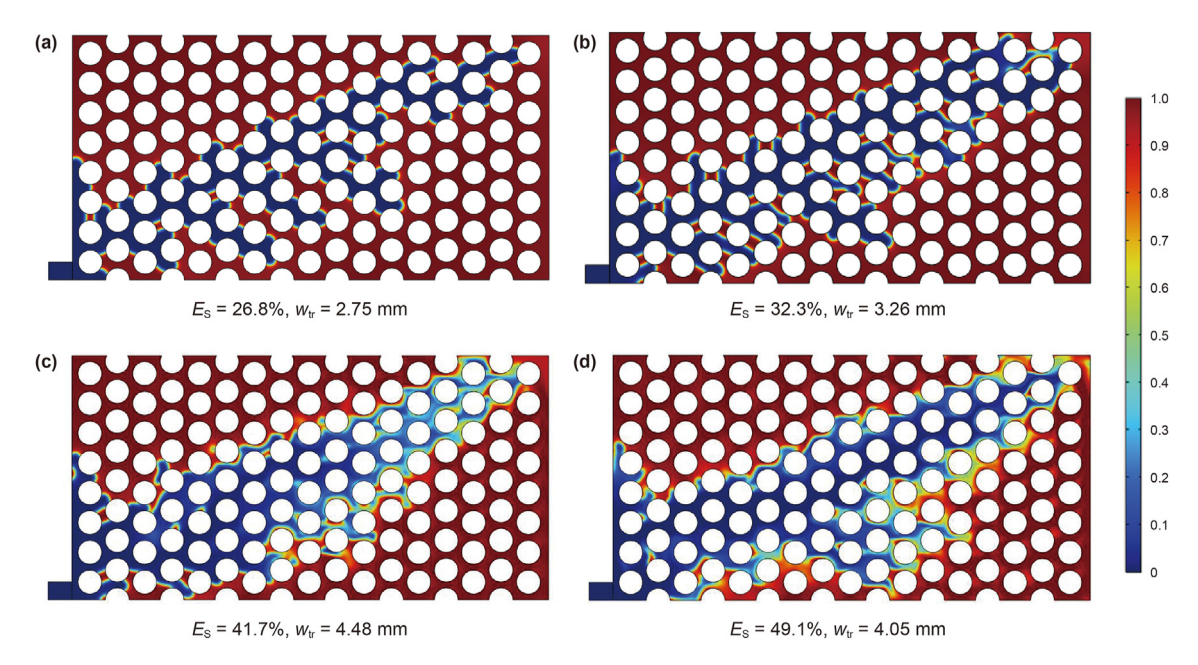


**Fig. 12.** Immiscible two-phase fluid distribution diagram of fingering by injection velocity ( $v_{in}$ ) based on the simulation model. (**a**) 0.01 mm/s; (**b**) 0.05 mm/s; (**c**) 0.25 mm/s; (**d**) 0.5 mm/s.

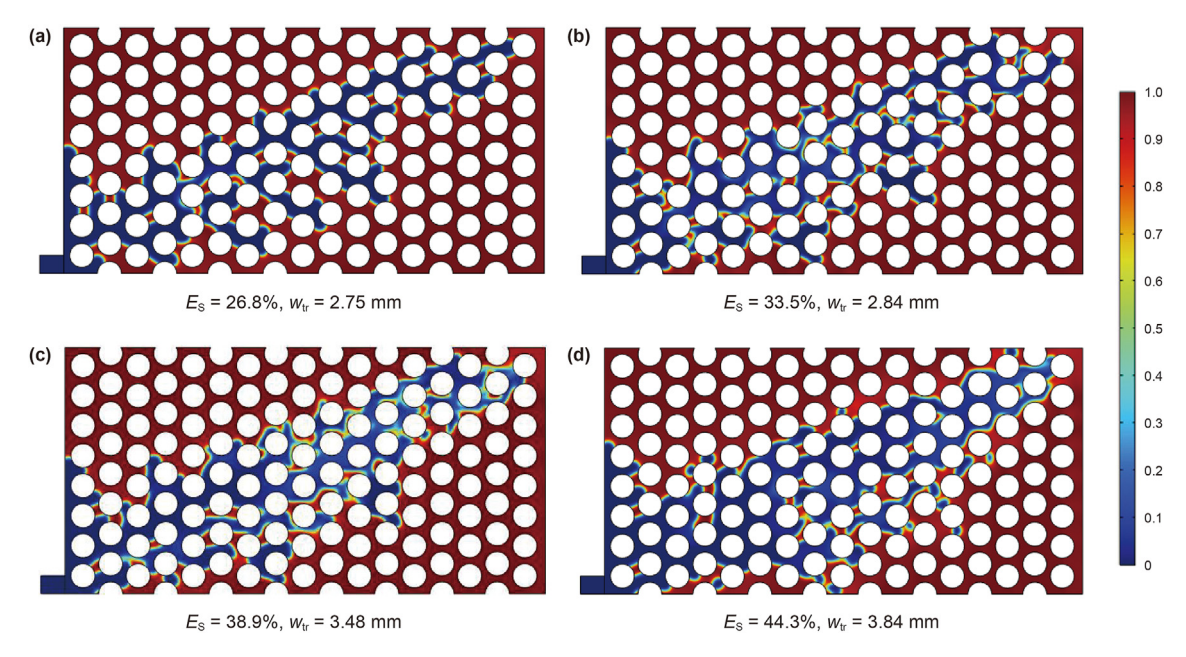


Fig. 13. Immiscible two-phase fluid distribution diagram of fingering by the IFT ( $\sigma_{in\text{-de}}$ ) based on the simulation model. (a) 30 mN/m; (b) 6 mN/m; (c) 1.2 mN/m; (d) 0.6 mN/m.

a miscible case as an extreme scenario of immiscibility, where the IFT approaches zero. Therefore, it is not necessary for the IFT to reach an ultra-low value in the simulation of miscible flow (Wang et al., 2020).

At the great interfacial intension, the width of the invasive trunk and branches were similar as shown in Fig. 13(a). By reducing the IFT to one-tenth, one-hundredth, or even one-thousandth of the initial value, it becomes apparent that the region extended by the invasive branch gradually succumbed to occupation by the invasive trunk. This reduction in IFT directly resulted in a significant expansion of the invasive width in the region near the outlet, facilitating defensive fluid leakage. It also emulates an experimental result: the change in the width of invasive trunk is

proportional to the IFT.

# 3.3.3. Fingering affected by viscosity

The viscosity ratio is a pivotal parameter for invasive patterns. The morphology of invasive branches and trunk under the same injection volume was observed by simulation method as shown in Fig. 14.

At the lowest viscosity ratio, fingering phenomenon manifested as a slender invasive trunk with numerous branches as shown in Fig. 14(a). The burst distance of invasive branches progressively diminished along the inlet-outlet lines. However, the boundaries among the various branches were clear and independent of each other. With the increase in viscosity ratio, the invasive trunk and

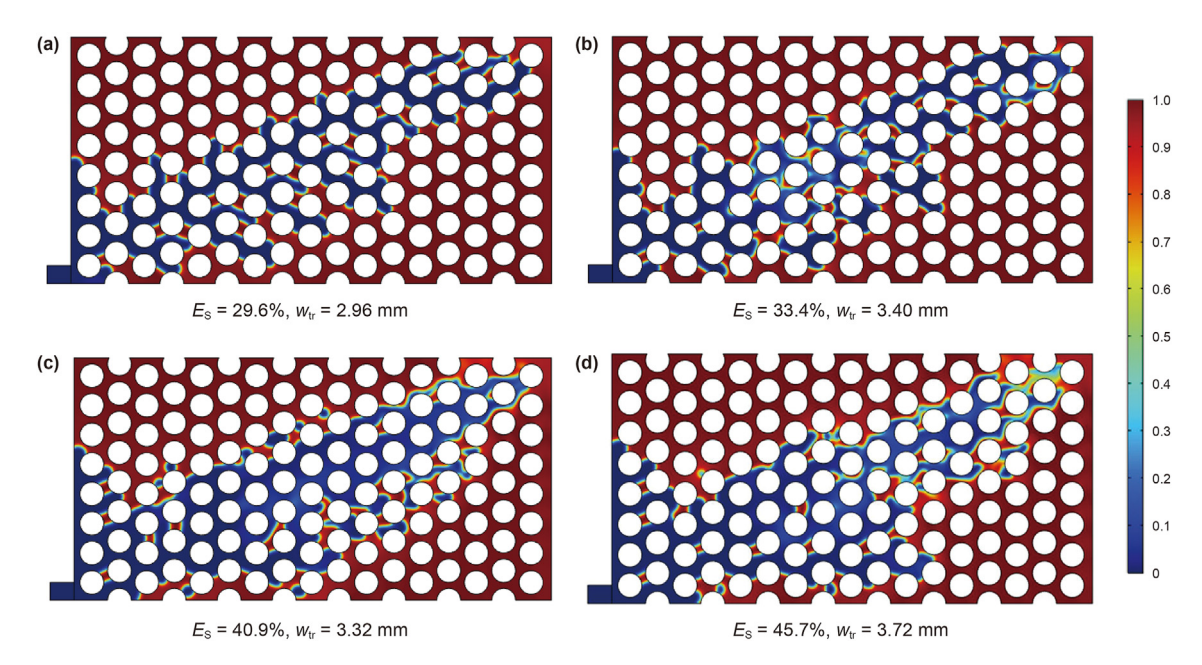


Fig. 14. Immiscible two-phase fluid distribution diagram of fingering by viscosity ratio (V<sub>in-de</sub>) based on the simulation model. (a) 0.01; (b) 0.05; (c) 0.25; (d) 0.5.

branches gradually fused, resulting in a large-width trunk and branches with shorter burst length. Simultaneously, the saturation of defensive fluid at the invasive interface gradually became great. The width of the invasive interface gradually decreases from the region near the inlet to the region near the outlet as shown in Fig. 14(c). At the greatest viscosity ratio, the saturation of defensive fluid near the region near the outlet also maintained a relatively high level because the much of invasive fluid was retained in the region near the inlet.

# 3.3.4. Fingering affected by capillary number

The above simulations individually vary the velocity, IFT and viscosity to investigate the influence on the sweep efficiency of the

fingering, but these parameters synergically affect the capillary number. There are also multiple parameter combinations for the constant capillary number. Compared with previous experiments, the viscosity and IFT at the invasive interface were more stable in the simulation. In this section, the novelty not only qualitatively analyzes the evolution of the invasive pattern but also quantitatively evaluates the extraction performance of the defensive fluid through sweep efficiency.

The change of injection velocity, invasive viscosity and IFT maintained a constant capillary number. The typical values of capillary number were conducted to present the interfacial morphology and sweep efficiency. In the comparison of various scenarios, the injection velocity decreased while the viscosity

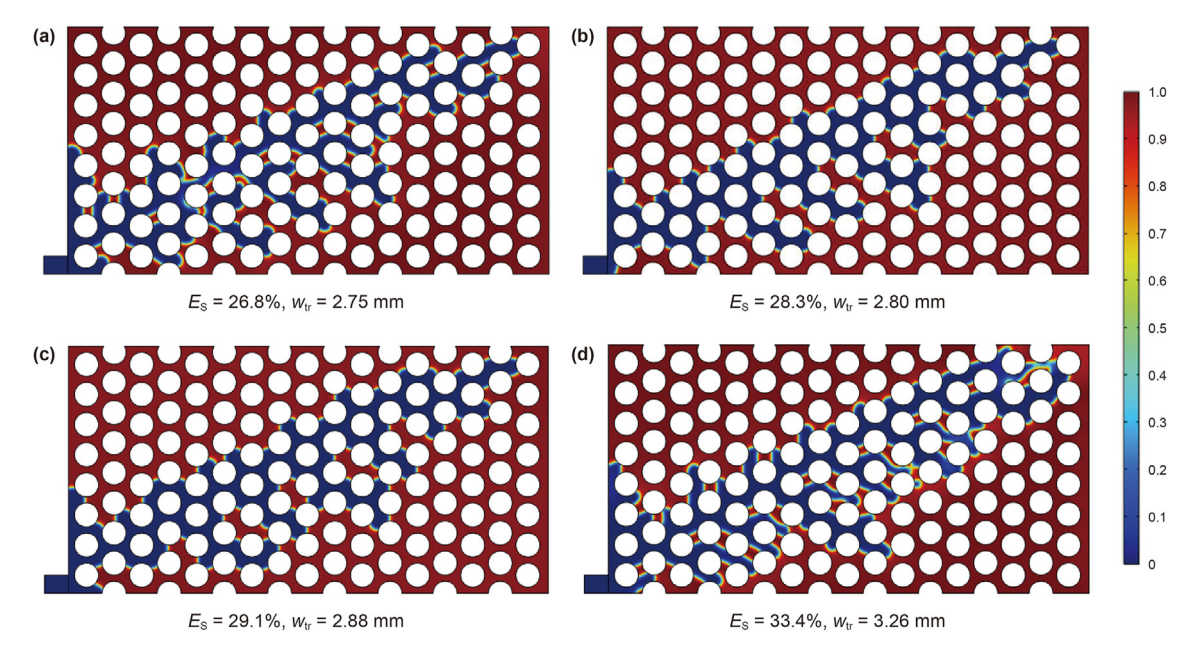


**Fig. 15.** Immiscible two-phase fluid distribution diagram of fingering at the constant capillary number (ln Ca = -12.0) with various parameters ( $v_{in}$  in mm/s,  $\mu_{in}$  in mPa s, and  $\sigma_{in\text{-de}}$  in mN/m). (a) 0.1, 0.1, and 30; (b) 0.01, 0.3, and 9; (c) 0.001, 3, and 9; (d) 0.0005, 10, and 15.

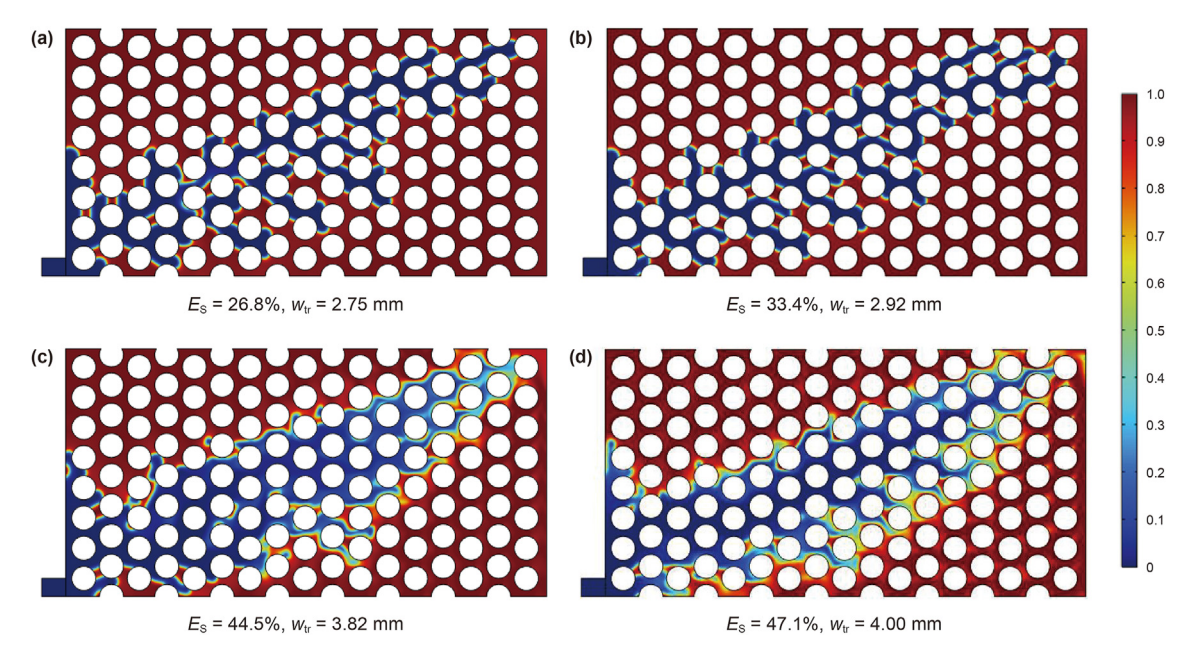


**Fig. 16.** Immiscible two-phase fluid distribution diagram of fingering at the constant capillary number (ln Ca=-8.1) with various parameters ( $v_{in}$  in mm/s,  $\mu_{in}$  in mPa s, and  $\sigma_{in-de}$  in mN/m). (a) 0.5, 0.1, and 3; (b) 0.25, 0.4, and 6; (c) 0.05, 1.5, and 4.5; (d) 0.005, 2, and 0.6.

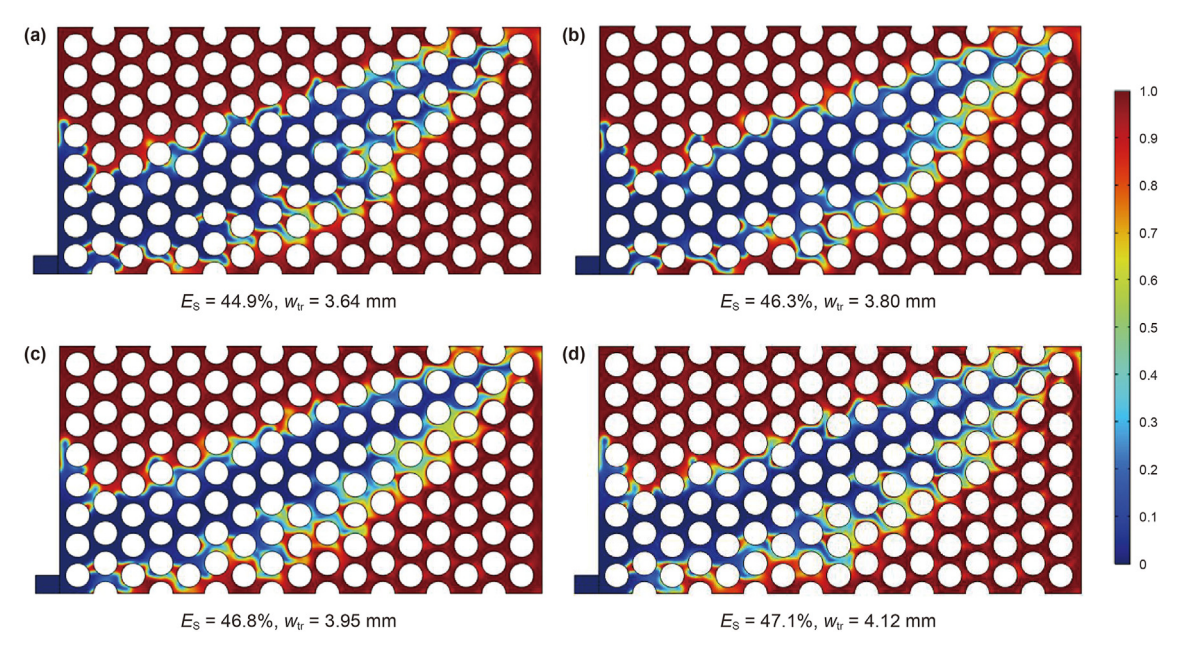


**Fig. 17.** Immiscible two-phase fluid distribution diagram of fingering at the constant capillary number (ln Ca=-4.1) with various parameters ( $v_{in}$  in mm/s,  $\mu_{in}$  in mPa s, and  $\sigma_{in-de}$  in mN/m). (a) 5, 2, and 3; (b) 1, 4, and 12; (c) 0.1, 5, and 1.5; (d) 0.05, 6, and 0.9.

increased as shown in Figs. 15–17.

Under the condition of low capillary number, the invasive pattern obviously presented the characteristics of multi-directional development, resulting from the invasive branches generated by capillary fingering. As the invasive viscosity increases, the density of invasive branches rises, subsequently enhancing sweep efficiency. Moreover, the spacing between different invasive branches gradually diminishes, although the increase in horizontal burst distance is not substantial.

Under the condition of crossover from capillary fingering to

viscous fingering, the invasive pattern reversed as the invasive velocity decreased and invasive viscosity increased. At great velocity and low viscosity, the invasive branches sufficiently extended to present the characteristics of multi-directional capillary fingering. Concurrently, the invasive trunk underwent gradual narrowing as it extended from the region near the inlet to the region near the outlet, indicating heightened control over unidirectional viscous fingering. Despite a consistent invasive pattern, reducing injection velocity and increasing invasive viscosity can lead to enhanced sweep efficiency. In comparison with Fig. 16(c)

and (d), an elevation in viscosity did not lead to a significant increase in the sweep efficiency. Conversely, a reduction in IFT fostered an augmentation of the sweep efficiency, concurrently resulting in a decrease in the width change of the invasive interface.

Under the condition of great capillary number, the invasive pattern obviously presented the characteristics of unidirectional development, resulting from the invasive trunk generated by viscous fingering. At the edge of the invasive trunk, the invasive branches exhibited extremely small burst distances. Furthermore, these branches can be assimilated by the invasive trunk, facilitating a straightforward increase in its width.

# 3.4. Analysis of invasive patterns

Based on the results from both experimental and simulation models, with the increase in capillary number and invasive distance, invasive branches generated by lateral expansion of capillary fingering are progressively assimilated into the invasive trunk. An immiscible two-phase flow equation is established to describe the variation of the fingering characteristics with the invasive distance. The applicable conditions for the two-phase flow equation can be clarified by the following assumptions: (1) both fluids and rock are incompressible; (2) only piston-like invasive process occurs in the pore space; (3) the parameters of flowing region, such as wettability and permeability, are isotropic; (4) fluids obey the Darcy flow equation; (5) only the inlet and outlet boundaries are open, and the rest are closed. According to the Laplace equation and Darcy's law of two-phase fluids in homogeneous circular model (Pinilla et al., 2021), the constitutive equation of invasive interface and the velocity potential controlled by pressure associated with pressure can be expressed as

$$\begin{cases} v_{i} = \lambda_{i}(dP_{i}/dr) + \lambda_{i}A\rho_{i}g\sin\alpha \\ \Phi = \lambda_{i}P & (i = 1,2) \\ \lambda_{i} = K_{i}/\mu_{i} & \end{cases}$$
(10)

where  $v_i$  represents the fluid velocity; i = 1, 2 separately represents the invasive fluid and defensive fluid;  $\lambda$  represents the mobility of fluid;  $\lambda$  represents the area of the flow section;  $\rho_i$  represents the

$$\Phi_{\rm r} = (v_i - \lambda_i A \rho_i g \sin \alpha) r + C \tag{11}$$

In mathematical model of fingering, it is assumed that the invasive fluid changes into the defensive fluid instantaneously at the invasive front. The pressure of inlet is set as  $P_{\rm in}$  and the pressure of outlet is set as  $P_{\rm wf}$ . Thus, the boundary equation of velocity potential can be expressed as

$$\begin{cases}
\Phi_{\text{in}} = \lambda_1 \cdot P|_{r=r_{\text{in}}} = \lambda_1 \cdot P_{\text{in}} \\
\Phi_{\text{ou}} = \lambda_2 \cdot P|_{r=r_{\text{ou}}} = \lambda_2 \cdot P_{\text{ou}}
\end{cases}$$
(12)

The velocity potential exerted by the fluid on both sides of the invasive interface is same. In addition, the simultaneous inlet and outlet boundary conditions for the establishment of equations can be expressed as

$$\begin{cases} \Phi_{\rm in} = (\nu_1 - \lambda_1 A \rho_1 g \sin \alpha) r_{\rm in} + C \\ \Phi_{\rm f} = (\nu_1 - \lambda_1 A \rho_1 g \sin \alpha) r_{\rm f} + C \\ \Phi_{\rm ou} = (\nu_2 - \lambda_2 A \rho_2 g \sin \alpha) r_{\rm ou} + C \\ \Phi_{\rm f} = (\nu_2 - \lambda_2 A \rho_2 g \sin \alpha) r_{\rm f} + C \end{cases}$$

$$(13)$$

where  $r_{\rm f}$  represents the distance between the invasive interface and the inlet point;  $r_{\rm in}$  represents the distance between the inlet and the inlet point;  $r_{\rm wf}$  represents the distance between the outlet and the inlet point.

The above equation can be further expressed as

$$\Phi_{\text{ou}} - \Phi_{\text{in}} = v_1 \left( r_f - r_{\text{in}} \right) + v_2 \left( r_{\text{ou}} - r_f \right) + \left[ \lambda_1 \rho_1 \left( r_{\text{in}} - r_f \right) + \lambda_2 \rho_2 \left( r_f - r_{\text{ou}} \right) \right] Ag \sin \alpha \tag{14}$$

Given the presence of different fluids flanking the invasive interface, it is imperative to augment the fluid transition with interface boundary conditions. In instances involving two slightly compressible or incompressible fluids, the pressure difference across the invasive interface can be considered constant. Under the condition of inlet and outlet at the same height, gravitational potential can be ignored. Furthermore, the velocity of defensive interface can be eliminated to express the velocity of the invasive fluid with the position of the invasive interface as shown

$$v_{1}|_{r=r_{f}} = \frac{\lambda_{2}P_{\text{ou}} - \lambda_{1}P_{\text{in}} - \left[\lambda_{2}(\rho_{2} - \rho_{1}) + \lambda_{1}\rho_{1}\left(r_{\text{in}} - r_{f}\right) + \lambda_{2}\rho_{2}\left(r_{f} - r_{\text{ou}}\right)\right]Ag \sin\alpha|_{\alpha=0}}{(1 - \lambda_{2}/\lambda_{1})r_{f} + \lambda_{2}\left/\lambda_{1} \cdot r_{\text{ou}} - r_{\text{in}}\right} = \frac{\lambda_{2}P_{\text{ou}} - \lambda_{1}P_{\text{in}}}{(1 - \lambda_{2}/\lambda_{1}) \cdot r_{f} + \lambda_{2}\left/\lambda_{1} \cdot r_{\text{ou}} - r_{\text{in}}\right|}$$

$$(15)$$

density of the fluid;  $\alpha$  represents the horizontal angle of the model;  $K_i$  represents the permeability and  $\mu_i$  represents the viscosity of the fluid

The velocity potential can be expressed as an integral of velocity:

The difference of invasive distance caused by the change of invasive velocity in the radial direction results in the rapid advance of the invasive interface. The growth rate of invasive distance can be expressed as

$$\frac{\mathrm{d}\delta}{\mathrm{d}\tau} = v_{1}|r = r_{f} + \Delta\delta - v_{1}|_{r=r_{f}}$$

$$= \frac{\lambda_{1}P_{\mathrm{in}} - \lambda_{2}P_{\mathrm{ou}}}{(1 - \lambda_{2}/\lambda_{1}) \cdot (r_{f} + \delta) + \lambda_{2}/\lambda_{1} \cdot r_{\mathrm{ou}} - r_{\mathrm{in}}} - \frac{\lambda_{1}P_{\mathrm{in}} - \lambda_{2}P_{\mathrm{ou}}}{(1 - \lambda_{2}/\lambda_{1}) \cdot r_{f} + \lambda_{2}/\lambda_{1} \cdot r_{\mathrm{ou}} - r_{\mathrm{in}}}$$

$$\approx \frac{(\lambda_{2}/\lambda_{1} - 1) \cdot \delta \cdot (\lambda_{1}P_{\mathrm{in}} - \lambda_{2}P_{\mathrm{ou}})}{\left[(1 - \lambda_{2}/\lambda_{1}) \cdot r_{f} + \lambda_{2}/\lambda_{1} \cdot r_{\mathrm{ou}} - r_{\mathrm{in}}\right]^{2}}$$

$$= \frac{(\lambda_{2}/\lambda_{1} - 1) \cdot \delta \cdot (\Phi_{\mathrm{in}} - \Phi_{\mathrm{ou}})}{\left[(1 - \lambda_{2}/\lambda_{1}) \cdot r_{f} + \lambda_{2}/\lambda_{1} \cdot r_{\mathrm{ou}} - r_{\mathrm{in}}\right]^{2}}$$
(16)

where  $\delta$  represents the burst length of invasive interface;  $\tau$  represents the invasive time of the burst length.

The mobility ratio ( $M = \lambda_2/\lambda_1$ ) is used to analyze the change rate of invasive interface as shown:

$$\begin{split} \eta &= \frac{\mathrm{d}\delta}{\delta\mathrm{d}\tau} \approx \frac{(\lambda_{2}/\lambda_{1} - 1)(\Phi_{\mathrm{in}} - \Phi_{\mathrm{ou}})}{\left[\left(r_{\mathrm{f}} - r_{\mathrm{in}}\right) + \lambda_{2}/\lambda_{1} \cdot \left(r_{\mathrm{ou}} - r_{\mathrm{f}}\right)\right]^{2}} \\ &= \frac{\Phi_{\mathrm{in}} - \Phi_{\mathrm{ou}}}{\left(r_{\mathrm{ou}} - r_{\mathrm{in}}\right)^{2}} \cdot \frac{\lambda_{2}/\lambda_{1} - 1}{\left[r_{\mathrm{D}} + \lambda_{2}/\lambda_{1} \cdot (1 - r_{\mathrm{D}})\right]^{2}} = C_{\mathrm{p}} \cdot \frac{M - 1}{\left[r_{\mathrm{D}} + (1 - r_{\mathrm{D}})M\right]^{2}} \end{split}$$
(17)

where  $\eta$  represents the mutation ratio of invasive interface;  $C_{\rm p}$  represents the potential constant per unit distance, which must be greater than zero;  $r_{\rm D}$  represents the dimensionless radius of the invasive interface,  $r_{\rm D} = r_{\rm f} / (r_{\rm wf} - r_{\rm in})$ . When the  $C_{\rm p}$  was set as 1, the mutation ratio of invasive interface can be displayed as Fig. 18(a).

The mutation ratio of viscous fingering evidently rises with the distance of the invasive interface from the inlet. Moreover, the invasive distance induced by viscous fingering needs to verify the progressively narrow invasive interface in the experimental and simulated results. The value of micro invasive distance can be obtained by integrating the mutation ratio of invasive interface as shown:

$$\int_{r_{\rm f}}^{r_{\rm f}+\Delta\delta} \frac{{\rm d}\delta}{\delta} = \int_{\tau_{\rm f}}^{\tau_{\rm f}+\Delta\tau} \eta {\rm d}\tau \tag{18}$$

After integrating, the burst length of the invasive interface can be expressed as

$$\Delta \delta = r_{\rm f}(e^{\eta \Delta \tau} - 1) = (r_{\rm ou} - r_{\rm in})r_{\rm D}\left(e^{\frac{(M-1)c_{\rm p}\Delta \tau}{[r_{\rm D} + (1-r_{\rm D})M]^2}} - 1\right)$$
(19)

When  $C_p\Delta \tau$  was set as 1, the burst length of the invasive interface can be shown as Fig. 18(b). When the distance was less than 0.9 times the inlet-outlet distance, the burst length width of the invasive interface generated by viscous fingering experiences a slight variation. Conversely, in regions proximate to the outlet, a consistent injection velocity resulted in a longer burst distance and a narrower invasive interface. The mathematical result of the

invasive interface implies that as the invasive interface develops more rapidly away from the inlet, resulting in a conical appearance of the invasive interface in the region near the outlet, which corresponds to Fig. 10(c).

For the burst width of the invasive interface, the invasive volume generated by constant flow rate at a fixed invasive time is constant. Based on the constant invasive volume, the variation trend of the invasive width can be shown as

$$\frac{v_1 \cdot \Delta \tau}{h} = \Delta \delta \cdot \frac{w|r = r_{f + \Delta \delta} + w|_{r = r_f}}{2}$$
 (20)

Where h represents the thickness of Hele–Shaw sand-packed model. The average invasive width in the burst element at the invasive interface can be expressed as

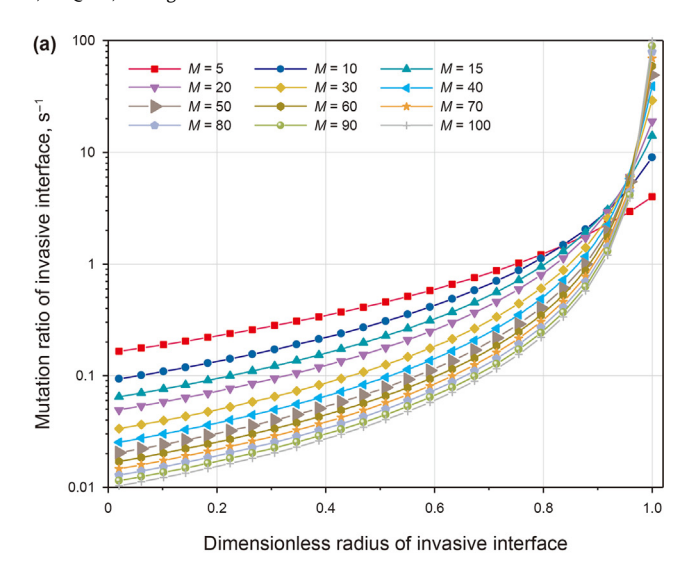
$$\frac{w|r = r_{f+\Delta\delta} + w|_{r=r_f}}{2} = \overline{w}\Delta\delta$$

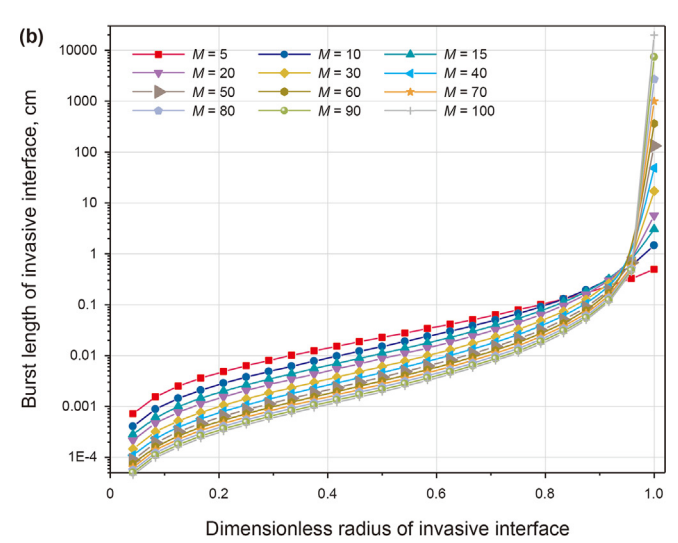
$$= \frac{\Delta Q_1}{h \cdot (r_{ou} - r_{in})} \cdot \frac{e^{\frac{[r_D + (1-r_D)M]^2}{(M-1)C_D\Delta r}}}{r_D \cdot \left(1 - e^{\frac{[r_D + (1-r_D)M]^2}{(M-1)C_D\Delta r}}\right)}$$
(21)

When  $\Delta Q_1/h\cdot(r_{ou}-r_{in})$  was set as 1, the burst length of the invasive interface can be displayed as Fig. 18(c). In the viscous fingering pattern, the burst width at the invasive interface showed a tendency to expand further in the region near the inlet, while it showed a tendency to decrease rapidly in the region near the outlet when viewed from the perspective of the invasive interface location

The experimental and theoretical models perform a good match in the burst length and width overall. In detail, the agreement between the two results regarding burst distance is imperfect for larger dimensionless radius values. Conversely, for smaller dimensionless radius values, the agreement between the two results regarding burst width is imperfect as shown in Fig. 19.

The phase diagram of invasive pattern evolution shows the various invasive patterns based on the displacement experiments in the glass micromodels, including the stable invasion, viscous fingering, capillary fingering, and crossover area (Chen et al., 2018). In the homogeneous hydrophilic pore space, the transition in the crossover area among the three typical invasive patterns was fuzzy.





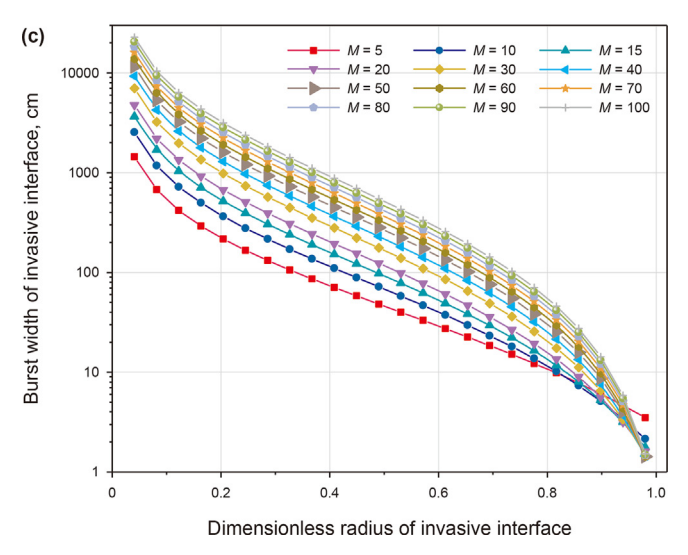


**Fig. 18.** Relationship of viscous fingering characteristics with dimensionless radius of invasive interface. (**a**) Mutation ratio; (**b**) Burst length; (**c**) Burst width.

In addition, both the physical and numerical models with multipore structures presented significant variations in fluid saturation. Each saturation of the wetting fluid corresponds to different mobility ratios. Hence, the mobility ratio is a highly intricate parameter in the multi-pore model and is unsuitable as a horizontal coordinate. Based on viscosity ratio and capillary number as independent variables, controlled by injection conditions and defensive fluid properties, the phase diagram of invasive pattern can be shown as Fig. 20.

In the invasive interface controlled by capillary fingering, invasive branches near the inlet immensely expand the extension region, albeit with narrower width and shorter distance compared to the invasive trunk. With a suitable increase in capillary number under a low viscosity ratio, the width of invasive branches gradually thickens, accompanied by a reduction in burst distance. As the capillary number increases further, the invasive branches initially merged into the invasive trunk from the outlet to the inlet. Once all of branches were merged into the trunk, the invasive characteristics of viscous fingering were ultimately presented. Under the condition of great capillary number, an increase in viscosity ratio, the width of the invasive trunk near the inlet increased further, but the invasive distance was reduced. Eventually, a stable invasive pattern was formed, leading to the uniform advancement of the invasive interface toward the outlet.

#### 4. Conclusions

We systematically characterized the various fingering pattern in porous media by performing a series of visualization experiments, two-phase flow model by employing finite element method. The major findings of this study are as follows.

- The fingering phenomenon is prone to manifest in porous media when the viscosity ratio and capillary fingering are low. At low capillary numbers, the invasive interface is inclined towards capillary fingering, characterized by multidirectional flow but narrow width. Conversely, at great capillary number, the invasive interface tends to be influenced by viscous fingering, featuring unidirectional flow but a broader width.
- In the capillary fingering pattern, the saturations of invasive fluid in the toe of the invasive branches surpass those at the heel. This observation implies that the invasive branches formed through capillary fingering exhibit a robust ability to extract the defensive fluid.
- In the fingering crossover pattern, the invasive interface near the inlet is mainly affected by capillary fingering, whereas the one near the outlet tends to be predominantly affected by viscous fingering. Decreasing invasive velocity, reducing interfacial tension, or increasing viscosity can enhance sweep efficiency, suggesting a stronger tendency toward viscous fingering pattern.
- In the viscous fingering pattern, the reduced interfacial tension results in diminished fluctuations in the width of the invasive interface, contributing to heightened stability. However, this stability adversely impacts the horizontal expansion of the invasive region.
- The burst distance of the invasive trunk exhibits a rapid increase as the invasive interface approaches the outlet, leading to a corresponding decrease in the width of the invasive interface.

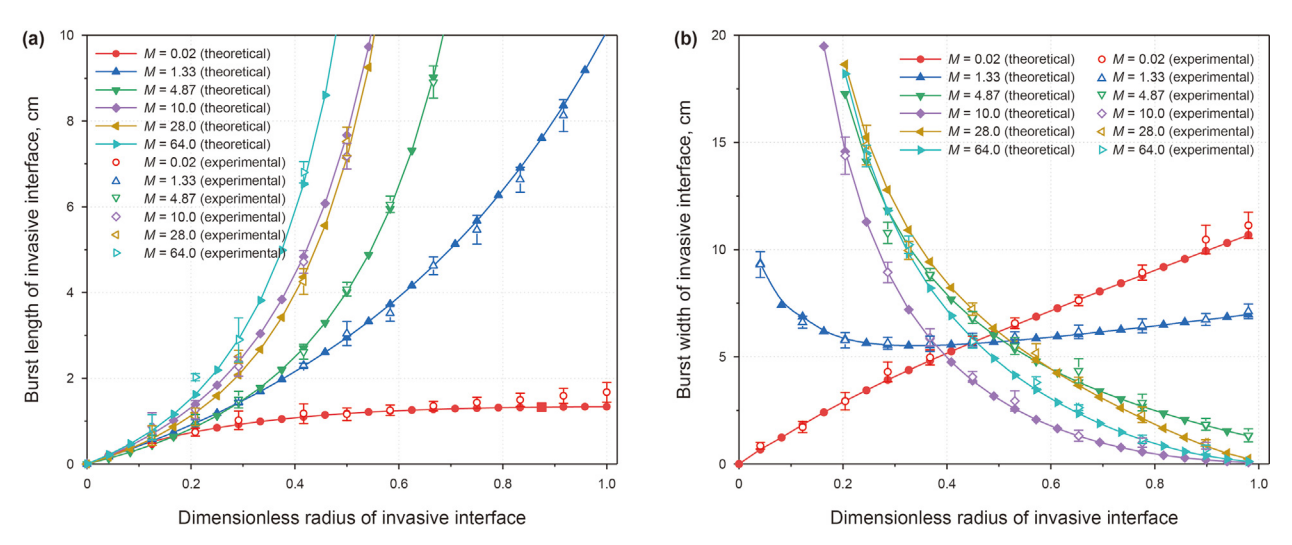


Fig. 19. Comparison of experimental and theoretical values in the invasive trunk. (a) Burst length; (b) Burst width.

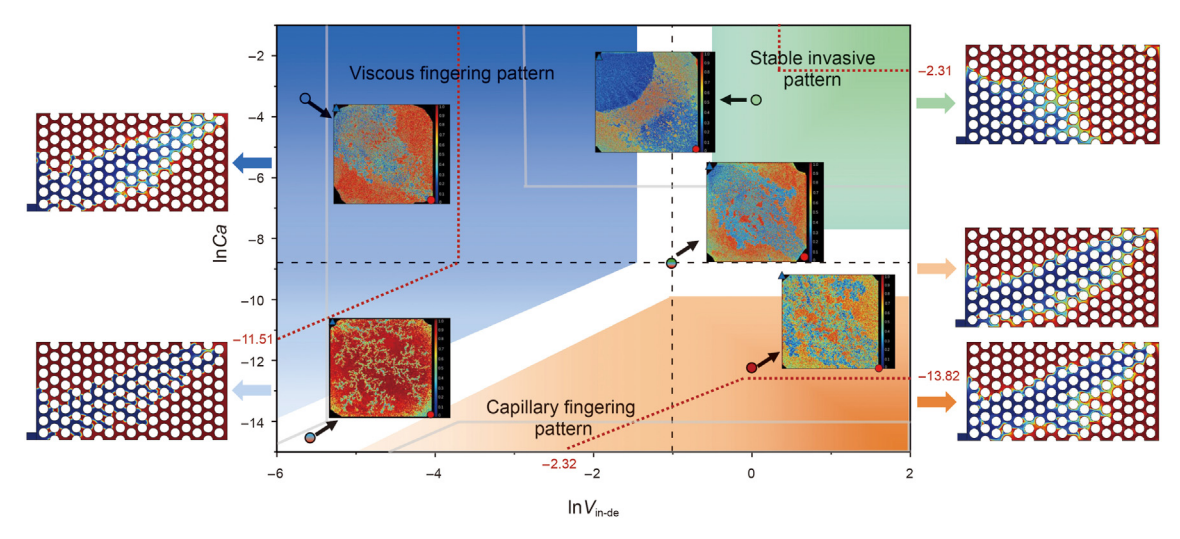


Fig. 20. Phase diagram for various invasive patterns from the numerical and experimental models. The reddish lines indicated by Lenormand et al. (1988), and the gray lines indicated by Guo and Aryana (2019).

# **CRediT authorship contribution statement**

Yu Li: Writing — original draft, Methodology, Investigation. Hui-Qing Liu: Supervision. Chao Peng: Writing — review & editing, Conceptualization. Peng Jiao: Validation, Methodology. Wai Lam Loh: Writing — review & editing. Qing Wang: Software, Investigation.

#### **Declaration of competing interest**

The authors declare that they have no known competing financial interests or personal relationships that could have appeared to influence the work reported in this paper.

# Acknowledgments

The research was supported by the National Natural Science Foundation of China Joint Fund Project (Grant/Award Number: U20B6003) and National Natural Science Foundation of China (Grant/Award Number: 52304054).

#### References

An, S., Erfani, H., Godinez-Brizuela, O.E., et al., 2020. Transition from viscous fingering to capillary fingering: application of GPU-based fully implicit dynamic pore network modeling. Water Resour. Res. 56, e2020WR028149. https:// doi.org/10.1029/2020WR028149.

Aryana, S.A., Kovscek, A.R., 2012. Experiments and analysis of drainage displacement processes relevant to carbon dioxide injection. Phys. Rev. 86, 066310. https://doi.org/10.1103/PhysRevE.86.066310.

Barenblatt, G., Patzek, T., Silin, D., 2003. The mathematical model of nonequilibrium effects in water-oil displacement. SPE J. 8, 409–416. https://doi.org/10.2118/87329-PA.

Bikkina, P., Wan, J., Kim, Y., et al., 2016. Influence of wettability and permeability heterogeneity on miscible CO<sub>2</sub> flooding efficiency. Fuel 166, 219–226. https://doi.org/10.1016/j.fuel.2015.10.090.

Bischofberger, I., Ramachandran, R., Nagel, S.R., 2014. Fingering versus stability in the limit of zero interfacial tension. Nat. Commun. 5, 5265. https://doi.org/ 10.1038/ncomms6265.

Blunt, M.J., Jackson, M.D., Piri, M., Valvatne, P.H., 2002. Detailed physics, predictive capabilities and macroscopic consequences for pore-network models of multiphase flow. Adv. Water Resour. 25, 1069–1089. https://doi.org/10.1016/S0309-1708(02)00049-0.

Brandão, R., Dias, E.O., Miranda, J.A., 2018. Immiscible three-dimensional fingering in porous media: a weakly nonlinear analysis. Physical Review Fluids 3, 034002. https://doi.org/10.1103/PhysRevFluids.3.034002.

Bruns, F., Babadagli, T., 2020. Heavy-oil recovery improvement by additives to steam injection: identifying underlying mechanisms and chemical selection through visual experiments. J. Petrol. Sci. Eng. 188, 106897. https://doi.org/10.1016/

j.petrol.2019.106897.

- Chang, C., Kneafsey, T.J., Wan, J., et al., 2020. Impacts of mixed-wettability on brine drainage and supercritical CO<sub>2</sub> storage efficiency in a 2.5D heterogeneous micromodel. Water Resour. Res. 56, e2019WR026789. https://doi.org/10.1029/ 2019WR026789
- Chen, Y.F., Fang, S., Wu, D.S., et al., 2017. Visualizing and quantifying the crossover from capillary fingering to viscous fingering in a rough fracture. Water Resour. Res. 53, 7756–7772. https://doi.org/10.1002/2017WR021051.
- Chen, Y.F., Guo, N., Wu, D.S., et al., 2018. Numerical investigation on immiscible displacement in 3D rough fracture: comparison with experiments and the role of viscous and capillary forces. Adv. Water Resour. 118, 39–48. https://doi.org/ 10.1016/j.advwatres.2018.05.016.
- Cottin, C., Bodiguel, H., Colin, A., 2010. Drainage in two-dimensional porous media: from capillary fingering to viscous flow. Phys. Rev. 82, 046315. https://doi.org/ 10.1103/PhysRevE.82.046315.
- Cui, G., Liu, M., Dai, W., et al., 2019. Pore-scale modelling of gravity-driven drainage in disordered porous media. Int. J. Multiphas. Flow 114, 19—27. https://doi.org/ 10.1016/j.ijmultiphaseflow.2019.02.001.
- Fei, L., Qin, F., Zhao, J., et al., 2023. Lattice Boltzmann modelling of isothermal two-component evaporation in porous media. J. Fluid Mech. 955, A18. https://doi.org/10.1017/jfm.2022.1048.
- Ferrari, A., Jimenez-Martinez, J., Borgne, T.L., et al., 2015. Challenges in modeling unstable two-phase flow experiments in porous micromodels. Water Resour. Res. 51, 1381–1400. https://doi.org/10.1002/2014WR016384.
- Furtado, F., Pereira, F., 2003. Crossover from nonlinearity controlled to heterogeneity-controlled mixing in two-phase porous media flows. Comput. Geosci. 7, 115—135. https://doi.org/10.1023/A:1023586101302.
- Guo, F., Aryana, S.A., 2019. An experimental investigation of flow regimes in imbibition and drainage using a microfluidic platform. Energies 12, 1390. https://doi.org/10.3390/en1207139.
- Hassanizadeh, S.M., Gray, W.G., 1993. Thermodynamic basis of capillary pressure in porous media. Water Resour. Res. 29, 3389–3405. https://doi.org/10.1029/93WR01495
- Holtzman, R., 2016. Effects of pore-scale disorder on fluid displacement in partially-wettable porous media. Sci. Rep. 6, 36221. https://doi.org/10.1038/srep36221.
- Hu, R., Wan, J., Yang, Z., et al., 2018. Wettability and flow rate impacts on immiscible displacement: a theoretical model. Geophys. Res. Lett. 45, 3077–3086. https:// doi.org/10.1002/2017GL076600.
- Hu, Y., Patmonoaji, A., Zhang, C., et al., 2020. Experimental study on the displacement pat- terns and the phase diagram of immiscible fluid displacement in three-dimensional porous media. Adv. Water Resour. 140, 103584. https://doi.org/10.1016/j.advwatres.2020.103584.
- Huang, C., Dai, X., Shi, C., et al., 2021. A comprehensive experimental study on immiscible displacements in porous media: effects of capillary forces, viscous forces, wettability and pore geometries. J. Therm. Sci. 1–13. https://doi.org/ 10.1007/s11630-021-1424-5.
- Keable, D., Jones, A., Krevor, S., Muggeridge, A., Jackson, S.J., 2022. The effect of viscosity ratio and Peclet number on miscible viscous fingering in a Hele—Shaw cell: a combined numerical and experimental study. Transport Porous Media 143, 23–45. https://doi.org/10.1007/s11242-022-01778-4.
- Kim, M., Kim, K.Y., Han, W.S., et al., 2019. Density-driven convection in a fractured porous media: implications for geological CO<sub>2</sub> storage. Water Resour. Res. 55, 5852-5870. https://doi.org/10.1029/2019WR024822.
- Krevor, S., De Coninck, H., Gasda, S.E., et al., 2023. Subsurface carbon dioxide and hydro- gen storage for a sustainable energy future. Nat. Rev. Earth Environ. 4, 102–118. https://doi.org/10.1038/s43017-022-00376-8.
- Lei, T., Luo, K.H., 2021. Pore-scale simulation of miscible viscous fingering with dissolution reaction in porous media. Phys. Fluids 33. https://doi.org/10.1063/ 5.0045051.
- Lenormand, R., Touboul, E., Zarcone, C., 1988. Numerical models and experiments on immiscible displacements in porous media. J. Fluid Mech. 189, 165–187. https://doi.org/10.1017/S0022112088000953.
- Li, Y., Liu, H., Wang, W., et al., 2023. Microvisual investigation on steam-assisted heavy oil extraction behavior in heterogeneous porous media. Energy & Fuels 37, 11776–11786. https://doi.org/10.1021/acs.energyfuels.3c01668.
- Liu, M., Mostaghimi, P., 2017. High-resolution pore-scale simulation of dissolution in porous media. Chem. Eng. Sci. 161, 360–369. https://doi.org/10.1016/
- McDougall, S., Sorbie, K., 1993. The combined effect of capillary and viscous forces on waterflood displacement efficiency in finely laminated porous media. In: SPE Annual Technical Conference and Exhibition. https://doi.org/10.2118/26659-MS.
- Mejia, L., Mejia, M., Xie, C., et al., 2021. Viscous fingering of irreducible water during favorable viscosity two-phase displacements. Adv. Water Resour. 153, 103943. https://doi.org/10.1016/j.advwatres.2021.103943.
- Nand, S., Sharma, V., Das, S.K., et al., 2022. Effect of Hele—Shaw cell gap on radial viscous fingering. Sci. Rep. 12, 18967. https://doi.org/10.1038/s41598-022-22769-x.
- Patmonoaji, A., Muharrik, M., Hu, Y., et al., 2020. Three-dimensional fingering structures in immiscible flow at the crossover from viscous to capillary fingering. Int. J. Multiphas. Flow 122, 103147. https://doi.org/10.1016/j.ijmultiphaseflow.2019.103147.
- Patmonoaji, A., Hu, Y., Nasir, M., et al., 2021. Effects of dissolution fingering on mass trans- fer rate in three-dimensional porous media. Water Resour. Res. 57,

e2020WR029353. https://doi.org/10.1029/2020WR029353.

- Pinilla, A., Asuaje, M., Ratkovich, N., 2021. Experimental and computational advances on the study of viscous fingering: an umbrella review. Heliyon 7, e07614. https://doi.org/10.1016/j.heliyon.2021.e07614.
- Pratama, R.A., Babadagli, T., 2020. Wettability state and phase distributions during steam injection with and without chemical additives: an experimental analysis using visual micromodels. SPE Reservoir Eval. Eng. 23, 1133–1149. https://doi.org/10.2118/196253-PA.
- Riaz, A., Tchelepi, H.A., 2004. Linear stability analysis of immiscible two-phase flow in porous media with capillary dispersion and density variation. Physics of Fluids 16, 4727–4737. https://doi.org/10.1063/1.181251.
- Salmo, I.C., Sorbie, K., Skauge, A., Alzaabi, M., 2022. Immiscible viscous fingering: modelling unstable water—oil displacement experiments in porous media. Transport Porous Media 145, 291–322. https://doi.org/10.1007/s11242-022-01847-8.
- Shi, Z., Wang, Z., Gan, Y., 2021. Effects of topological disorder in unsaturated granular media via a pore-scale lattice Boltzmann investigation. Adv. Water Resour. 149, 103855. https://doi.org/10.1016/j.advwatres.2021.103855.
- Singh, M., Chaudhuri, A., Chu, S.P., et al., 2019. Analysis of evolving capillary transition, gravitational fingering, and dissolution trapping of CO<sub>2</sub> in deep saline aquifers during continuous injection of supercritical CO<sub>2</sub>. Int. J. Greenh. Gas Control 82, 281–297. https://doi.org/10.1016/j.ijggc.2019.01.014.
- Sorbie, K., Al Ghafri, A., Skauge, A., et al., 2020. On the modelling of immiscible viscous fingering in two-phase flow in porous media. Transport Porous Media 135, 331–359. https://doi.org/10.1007/s11242-020-01479-w.
- Tabrizinejadas, S., Fahs, M., Hoteit, H., et al., 2023. Effect of temperature on convective-reactive transport of CO<sub>2</sub> in geological formations. Int. J. Greenh. Gas Control 128, 103944. https://doi.org/10.1016/j.jiggc.2023.103944.
- Control 128, 103944. https://doi.org/10.1016/j.ijggc.2023.103944.

  Tang, Y., Li, M., Bernabé, Y., et al., 2020. Viscous fingering and preferential flow paths in heterogeneous porous media. J. Geophys. Res. Solid Earth 125, e2019JB019306. https://doi.org/10.1029/2019JB019306.
- Wang, C., Liu, Y., Du, Y., et al., 2021. Heavy-oil recovery by combined geothermal energy and cosolvent/water flooding. Energy 228, 120681. https://doi.org/ 10.1016/j.energy.2021.120681.
- Wang, S., Cheng, Z., Zhang, Y., et al., 2021. Unstable density-driven convection of CO<sub>2</sub> in homogeneous and heterogeneous porous media with implications for deep saline aquifers. Water Resour. Res. 57, e2020WR028132. https://doi.org/10.1029/2020WR028132.
- Wang, T., Wang, L., Wang, J., et al., 2022. In-situ emulsification synergistic self-profile control system on heavy oil reservoir development: prescription construction and EOR mechanism investigation. J. Petrol. Sci. Eng. 219, 111069. https://doi.org/10.1016/j.petrol.2022.111069.
- Wang, Y., Aryana, S.A., Allen, M.B., 2019. An extension of Darcy's law incorporating dynamic length scales. Adv. Water Resour. 129, 70–79. https://doi.org/10.1016/i.advwatres.2019.05.010.
- Wang, Z., Chauhan, K., Pereira, J.M., Gan, Y., 2019. Disorder characterization of porous media and its effect on fluid displacement. Physical Review Fluids 4, 034305. https://doi.org/10.1103/PhysRevFluids.4.034305.
- Wang, Z., Feyen, J., Elrick, D.E., 1998. Prediction of fingering in porous media. Water Resour. Res. 34, 2183–2190. https://doi.org/10.1029/98WR01472.
- Wei, H., Zhu, X., Liu, X., et al., 2022. Pore-scale study of drainage processes in porous media with various structural heterogeneity. Int. Commun. Heat Mass Tran. 132, 105914. https://doi.org/10.1016/j.icheatmasstransfer.2022.105914.
- Wu, Z., Wang, L., Xie, C., et al., 2019. Experimental investigation on improved heavy oil recovery by air assisted steam injection with 2D visualized models. Fuel 252, 109–115. https://doi.org/10.1016/j.fuel.2019.04.097.
- Yang, S., Kong, G., Cao, Z., et al., 2022. Hydrodynamics of gas-liquid displacement in porous media: fingering pattern evolution at the breakthrough moment and the stable state. Adv. Water Resour. 170, 104324. https://doi.org/10.1016/ i.advwatres.2022.104324.
- Yang, Z., Méheust, Y., Neuweiler, I., et al., 2019. Modeling immiscible two-phase flow in rough fractures from capillary to viscous fingering. Water Resour. Res. 55, 2033–2056. https://doi.org/10.1029/2018WR024045.
- Zakirov, T., Khramchenkov, M., 2020. Prediction of permeability and tortuosity in heterogeneous porous media using a disorder parameter. Chem. Eng. Sci. 227, 115893. https://doi.org/10.1016/j.ces.2020.115893.
- Zhang, H., Papadikis, K., Shaw, S.J., 2023. A two-dimensional transient study on the impact of pore space connectivity on the immiscible two-phase flow in a waterwet, water-oil system. Int. J. Multiphas. Flow 165, 104474. https://doi.org/ 10.1016/j.ijmultiphaseflow.2023.104474.
- Zhang, Y., Gai, C., Song, B., et al., 2023. The influence of permeability and heterogeneity on chemical flooding efficiency and remaining oil distribution-based on NMR displacement imaging. Sci. Rep. 13, 14316. https://doi.org/10.1038/s41598-023-39535-2.
- Zhao, B., Mohanty, K.K., 2019. Effect of wettability on immiscible viscous fingering in porous media. J. Petrol. Sci. Eng. 174, 738–746. https://doi.org/10.1016/ i.petrol.2018.11.072.
- Zhao, J., Yang, J., Zeng, F., 2023. Complex displacement behavior during foaming gas drainage in 2D microfluidic networks. Fuel 344, 128071. https://doi.org/10.1016/j.fuel.2023.128071.
- Zheng, X., Mahabadi, N., Yun, T.S., et al., 2017. Effect of capillary and viscous force on CO<sub>2</sub> saturation and invasion pattern in the microfluidic chip. J. Geophys. Res. Solid Earth 122, 1634–1647. https://doi.org/10.1002/2016JB013908.